

WL-TR-96-3061

**COMPUTATIONS OF SUPERSONIC
VORTICAL FLOWS AROUND OGIVE-
CYLINDERS USING CENTRAL AND
UPWIND DIFFERENCES**



ESWAR JOSYULA

MARCH 1997

FINAL REPORT FOR 1 JULY 1994 - 1 MARCH 1996

DTIC QUALITY INSPECTED 2

Approved for public release; distribution unlimited

FLIGHT DYNAMICS DIRECTORATE
WRIGHT LABORATORY
AIR FORCE MATERIEL COMMAND
WRIGHT-PATTERSON AIR FORCE BASE, OH 45433-7562

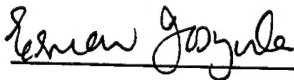
19970422 162

NOTICE

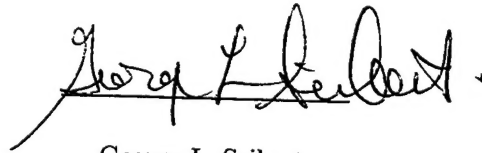
USING GOVERNMENT DRAWINGS, SPECIFICATIONS, OR OTHER DATA INCLUDED IN THIS DOCUMENT FOR ANY PURPOSE OTHER THAN GOVERNMENT PROCUREMENT DOES NOT IN ANY WAY OBLIGATE THE US GOVERNMENT. THE FACT THAT THE GOVERNMENT FORMULATED OR SUPPLIED THE DRAWINGS, SPECIFICATIONS, OR OTHER DATA DOES NOT LICENSE THE HOLDER OR ANY OTHER PERSON OR CORPORATION; OR CONVEY ANY RIGHTS OR PERMISSION TO MANUFACTURE, USE, OR SELL ANY PATENTED INVENTION THAT MAY RELATE TO THEM.

THIS REPORT IS RELEASABLE TO THE NATIONAL TECHNICAL INFORMATION SERVICE (NTIS). AT NTIS, IT WILL BE AVAILABLE TO THE GENERAL PUBLIC, INCLUDING FOREIGN NATIONS.

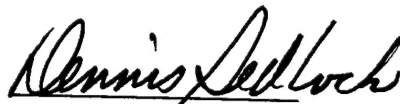
THIS TECHNICAL REPORT HAS BEEN REVIEWED AND IS APPROVED FOR PUBLICATION.



Eswar Josyula
Aerospace Engineer
CFD Research Section



George L. Seibert
Chief
CFD Research Branch



Dennis Sedlock
Chief
Aeromechanics Division

IF YOUR ADDRESS HAS CHANGED, IF YOU WISH TO BE REMOVED FROM OUR MAILING LIST, OR IF THE ADDRESSEE IS NO LONGER EMPLOYED BY YOUR ORGANIZATION PLEASE NOTIFY WL/FIMC, WRIGHT-PATTERSON AFB OH 45433-7913 TO HELP MAINTAIN A CURRENT MAILING LIST.

Do not return copies of this report unless contractual obligations or notice on a specific document requires its return.

REPORT DOCUMENTATION PAGE			Form Approved OMB No. 0704-0188	
Public reporting burden for this collection of information is estimated to average 1 hour per response, including the time for reviewing instructions, searching existing data sources, gathering and maintaining the data needed, and completing and reviewing the collection of information. Send comments regarding this burden estimate or any other aspect of this collection of information, including suggestions for reducing this burden, to Washington Headquarters Services, Directorate for Information Operations and Reports, 1215 Jefferson Davis Highway, Suite 1204, Arlington, VA 22202-4302, and to the Office of Management and Budget, Paperwork Reduction Project (0704-0188), Washington, DC 20503.				
1. AGENCY USE ONLY (Leave blank)	2. REPORT DATE MAR 1997	3. REPORT TYPE AND DATES COVERED FINAL REPORT, 07/01/94--03/01/96		
4. TITLE AND SUBTITLE Computations of Supersonic Vortical Flows Around Ogive-Cylinders Using Central and Upwind Differences		5. FUNDING NUMBERS PE 62201 PR 2307 TA N6 WU 11		
6. AUTHOR(S) Eswar Josyula		8. PERFORMING ORGANIZATION REPORT NUMBER		
7. PERFORMING ORGANIZATION NAME(S) AND ADDRESS(ES) FLIGHT DYNAMICS DIRECTORATE WRIGHT LABORATORY AIR FORCE MATERIEL COMMAND WRIGHT-PATTERSON AFB OH 45433-7562		10. SPONSORING / MONITORING AGENCY REPORT NUMBER WL-TR-96-3061		
9. SPONSORING / MONITORING AGENCY NAME(S) AND ADDRESS(ES) FLIGHT DYNAMICS DIRECTORATE WRIGHT LABORATORY AIR FORCE MATERIEL COMMAND WRIGHT-PATTERSON AFB OH 45433-7562 POC: ESWAR JOSYULA, 937-255-2455		11. SUPPLEMENTARY NOTES APPROVED FOR PUBLIC RELEASE; DISTRIBUTION IS UNLIMITED		
12a. DISTRIBUTION / AVAILABILITY STATEMENT APPROVED FOR PUBLIC RELEASE; DISTRIBUTION IS UNLIMITED		12b. DISTRIBUTION CODE		
13. ABSTRACT (Maximum 200 words) This work is part of a cooperative research, development, test and evaluation program that brings scientists and engineers from various English-speaking countries together for collaborative studies to improve technology to solve technical problems. The current TTCP work project WTP-2 KTA 2-12, "Application of CFD to the prediction of Missile Body Vortices" focuses on the ability of the three-dimensional Navier-Stokes equations to predict flowfields about high length-to-diameter bodies at moderate angles of attack ($8^\circ \leq \sigma \leq 14^\circ$) for supersonic Mach numbers. This report documents this author's computational results for the five test cases. The five test cases are as follows. Mach 1.45 at $\sigma = 14^\circ$, Mach 1.8 at $\sigma = 14^\circ$, Mach 2.5 at $\sigma = 14^\circ$, Mach 3.5 at $\sigma = 8^\circ$, and Mach 3.5 at $\sigma = 14^\circ$. The experimental body is 13 diameters long with the diameter of the cylindrical afterbody of 3.7 inches. Laminar and turbulent computations are shown with comparisons to experimental data. The experimental validation data was provided by the Defence Research Agency (UK). The computations were performed with an existing Navier-Stokes code FDL3DI developed in the Wright Laboratory. The surface pressure and pitot pressure predictions matched with the experimental data reasonably well. The k- ϵ Turbulence model was found to be highly dissipative for capturing vortical flows. Local grid refinement was considered to be an important aspect of capturing the vortical flows accurately.				
14. SUBJECT TERMS Missile Configuration, Computational Fluid Dynamics, Supersonic Flows, Vortical Flows		15. NUMBER OF PAGES 39		
		16. PRICE CODE		
17. SECURITY CLASSIFICATION OF REPORT UNCLASSIFIED	18. SECURITY CLASSIFICATION OF THIS PAGE UNCLASSIFIED	19. SECURITY CLASSIFICATION OF ABSTRACT UNCLASSIFIED	20. LIMITATION OF ABSTRACT SAR	

Table of Contents

List of Figures	iv
List of Tables	viii
Acknowledgement	xii
List of Abbreviations and Symbols	ix
1 Introduction	1
2 Analysis	3
2.1 Boundary Conditions	8
2.2 Experimental Data and Conditions of Numerical Simulation	8
2.3 Grid Study	10
3 Computer Requirements	11
4 Discussion of Results	13
4.1 Surface Pressure Comparisons for Case 3 on Standard Grid	13
4.2 Pitot Pressure Comparisons for Case 3 on Standard Grid	13
4.3 Pitot Pressure Comparisons for Cases 1 to 5	14
4.4 Surface Pressure Comparisons for Cases 1 to 5	15
4.5 Convergence History for Case 3 on Standard Grid	15
4.6 Forces and Moments for Case 3 on Standard Grid	15
5 Summary and Conclusions	17
6 References	19

List of Figures

1	Experimental Data Geometry	21
2	Computational Grid	21
3	Grid Study: Comparison of Pitot Pressure along Vortex Centerline for Laminar	21
4	Grid Study: Comparison of Pitot Pressure along Vortex Centerline for Turbulent	21
5	Comparison of Surface Pressure on Standard Grid at $X/D = 2.4$ for Laminar	22
6	Comparison of Surface Pressure on Standard Grid at $X/D = 2.4$ for Turbulent	22
7	Comparison of Surface Pressure on Standard Grid at $X/D = 3.5$ for Laminar	22
8	Comparison of Surface Pressure on Standard Grid at $X/D = 3.5$ for Turbulent	22
9	Comparison of Surface Pressure on Standard Grid $X/D = 4.5$ for Laminar	22
10	Comparison of Surface Pressure on Standard Grid $X/D = 4.5$ for Turbulent	22
11	Comparison of Surface Pressure on Standard Grid at $X/D = 5.5$ for Laminar	23
12	Comparison of Surface Pressure on Standard Grid at $X/D = 5.5$ for Turbulent	23
13	Comparison of Surface Pressure on Standard Grid at $X/D = 6.5$ for Laminar	23
14	Comparison of Surface Pressure on Standard Grid at $X/D = 6.5$ for Turbulent	23
15	Comparison of Surface Pressure on Standard Grid at $X/D = 7.5$ for Laminar	23
16	Comparison of Surface Pressure on Standard Grid at $X/D = 7.5$ for Turbulent	23
17	Comparison of Surface Pressure on Standard Grid at $X/D = 8.5$ for Laminar	24
18	Comparison of Surface Pressure on Standard Grid at $X/D = 8.5$ for Turbulent	24
19	Comparison of Surface Pressure on Standard Grid at $X/D = 11.5$ for Laminar	24
20	Comparison of Surface Pressure on Standard Grid at $X/D = 11.5$ for Turbulent	24
21	Comparison of Pitot Pressure on Standard Grid at $X/D = 5.5$ using Central Diff. (Laminar)	24
22	Comparison of Pitot Pressure on standard grid at $X/D = 5.5$ using Central Diff. (Turbulent)	25
23	Comparison of Pitot Pressure along Vortex Centerline using Standard Grid at $X/D = 5.5$ using Central Diff.	25
24	Comparison of Pitot Pressure on Standard Grid at $X/D = 5.5$ using Upwind Diff. (Laminar)	25
25	Comparison of Pitot Pressure on Standard Grid at $X/D = 5.5$ using Upwind Diff. (Turbulent)	25
26	Comparison of Pitot Pressure along Vortex Centerline using Standard Grid at $X/D = 5.5$ using Upwind Diff.	26
27	Comparison of Pitot Pressure on Standard Grid at $X/D = 11.5$ using Central Diff. (Laminar)	26
28	Comparison of Pitot Pressure on Standard Grid at $X/D = 11.5$ using Central Diff. (Turbulent)	26

29	Comparison of Pitot Pressure along Vortex Centerline using Standard Grid at $X/D = 11.5$ using Central Diff.	26
30	Comparison of Pitot Pressure on Standard Grid at $X/D = 11.5$ using Upwind Diff. (Laminar)	27
31	Comparison of Pitot Pressure on Standard Grid at $X/D = 11.5$ using Upwind Diff. (Turbulent)	27
32	Comparison of Pitot Pressure along Vortex Centerline using Standard Grid at $X/D = 11.5$ using Upwind Diff.	27
33	Comparison of Pitot Pressure for Case 1 at $X/D = 8.5$ (Laminar)	27
34	Comparison of Pitot Pressure for Case 1 at $X/D = 8.5$ (Turbulent)	28
35	Comparison of Pitot Pressure along Vortex Centerline for Case 1 at $X/D = 8.5$	28
36	Comparison of Pitot Pressure for Case 1 at $X/D = 11.5$ (Laminar)	28
37	Comparison of Pitot Pressure for Case 1 at $X/D = 11.5$ (Turbulent)	28
38	Comparison of Pitot Pressure along Vortex Centerline for Case 1 at $X/D = 11.5$	28
39	Comparison of Pitot Pressure for Case 2 at $X/D = 5.5$ (Laminar)	28
40	Comparison of Pitot Pressure for Case 2 at $X/D = 5.5$ (Turbulent)	29
41	Comparison of Pitot Pressure for Case 2 at $X/D = 8.5$ (Laminar)	29
42	Comparison of Pitot Pressure for Case 2 at $X/D = 8.5$ (Turbulent)	29
43	Comparison of Pitot Pressure along Vortex Centerline for Case 2 at $X/D = 8.5$	29
44	Comparison of Pitot Pressure for Case 2 at $X/D = 11.5$ (Laminar)	29
45	Comparison of Pitot Pressure for Case 2 at $X/D = 11.5$ (Turbulent)	29
46	Comparison of Pitot Pressure along Vortex Centerline for Case 2 at $X/D = 11.5$	30
47	Comparison of Pitot Pressure for Case 3 at $X/D = 5.5$ (Laminar)	30
48	Comparison of Pitot Pressure for Case 3 at $X/D = 5.5$ (Turbulent)	30
49	Comparison of Pitot Pressure for Case 3 at $X/D = 11.5$ (Laminar)	30
50	Comparison of Pitot Pressure for Case 3 at $X/D = 11.5$ (Turbulent)	30
51	Comparison of Pitot Pressure along Vortex Centerline for Case 3 at $X/D = 11.5$	30
52	Comparison of Pitot Pressure for Case 4 at $X/D = 11.5$ (Laminar)	31
53	Comparison of Pitot Pressure for Case 4 at $X/D = 11.5$ (Turbulent)	31
54	Comparison of Pitot Pressure along Vortex Centerline for Case 4 at $X/D = 11.5$	31
55	Comparison of Pitot Pressure for Case 5 at $X/D = 5.5$ (Laminar)	31
56	Comparison of Pitot Pressure for Case 5 at $X/D = 5.5$ (Turbulent)	31
57	Comparison of Pitot Pressure for Case 5 at $X/D = 11.5$ (Laminar)	31
58	Comparison of Pitot Pressure for Case 5 at $X/D = 11.5$ (Turbulent)	32

59	Comparison of Pitot Pressure along Vortex Centerline for Case 5 at $X/D = 11.5$	32
60	Comparison of Surface Pressure for Case 1 at $X/D = 2.4$	32
61	Comparison of Surface Pressure for Case 1 at $X/D = 3.5$	32
62	Comparison of Surface Pressure for Case 1 at $X/D = 4.5$	32
63	Comparison of Surface Pressure for Case 1 at $X/D = 5.5$	32
64	Comparison of Surface Pressure for Case 1 at $X/D = 6.5$	33
65	Comparison of Surface Pressure for Case 1 at $X/D = 7.5$	33
66	Comparison of Surface Pressure for Case 1 at $X/D = 3.5$	33
67	Comparison of Surface Pressure for Case 1 at $X/D = 11.5$	33
68	Comparison of Surface Pressure for Case 2 at $X/D = 2.4$	33
69	Comparison of Surface Pressure for Case 2 at $X/D = 3.5$	33
70	Comparison of Surface Pressure for Case 2 at $X/D = 4.5$	34
71	Comparison of Surface Pressure for Case 2 at $X/D = 5.5$	34
72	Comparison of Surface Pressure for Case 2 at $X/D = 6.5$	34
73	Comparison of Surface Pressure for Case 2 at $X/D = 7.5$	34
74	Comparison of Surface Pressure for Case 2 at $X/D = 8.5$	34
75	Comparison of Surface Pressure for Case 2 at $X/D = 11.5$	34
76	Comparison of Surface Pressure for Case 3 at $X/D = 2.4$	35
77	Comparison of Surface Pressure for Case 3 at $X/D = 3.5$	35
78	Comparison of Surface Pressure for Case 3 at $X/D = 4.5$	35
79	Comparison of Surface Pressure for Case 3 at $X/D = 5.5$	35
80	Comparison of Surface Pressure for Case 3 at $X/D = 6.5$	35
81	Comparison of Surface Pressure for Case 3 at $X/D = 7.5$	35
82	Comparison of Surface Pressure for Case 3 at $X/D = 8.5$	36
83	Comparison of Surface Pressure for Case 3 at $X/D = 11.5$	36
84	Comparison of Surface Pressure for Case 4 at $X/D = 2.4$	36
85	Comparison of Surface Pressure for Case 4 at $X/D = 3.5$	36
86	Comparison of Surface Pressure for Case 4 at $X/D = 4.5$	36
87	Comparison of Surface Pressure for Case 4 at $X/D = 5.5$	36
88	Comparison of Surface Pressure for Case 4 at $X/D = 6.5$	37
89	Comparison of Surface Pressure for Case 4 at $X/D = 7.5$	37
90	Comparison of Surface Pressure for Case 4 at $X/D = 8.5$	37

91	Comparison of Surface Pressure for Case 4 at $X/D = 11.5$	37
92	Comparison of Surface Pressure for Case 5 at $X/D = 2.4$	37
93	Comparison of Surface Pressure for Case 5 at $X/D = 3.5$	37
94	Comparison of Surface Pressure for Case 5 at $X/D = 4.5$	38
95	Comparison of Surface Pressure for Case 5 at $X/D = 5.5$	38
96	Comparison of Surface Pressure for Case 5 at $X/D = 5.5$	38
97	Comparison of Surface Pressure for Case 5 at $X/D = 7.5$	38
98	Comparison of Surface Pressure for Case 5 at $X/D = 8.5$	38
99	Comparison of Surface Pressure for Case 5 at $X/D = 11.5$	38
100	Convergence History for Laminar Computation	39
101	Convergence History for Turbulent Computation	39

List of Tables

2.1	Free Stream Conditions	9
2.2	Available Experimental Data	9
2.3	Details of grids considered in this study	10
3.1	Computer resources requirements	12
4.1	Comparison of Forces and Moments with Experiment for Central and Upwind Difference Versions for Case 3 on Standard Grid	16

List of Abbreviations and Symbols

$C_{\epsilon 1}$	=	turbulence model constant, 1.44
$C_{\epsilon 2}$	=	turbulence model constant, 1.92
C_D	=	Coefficient of Drag
C_L	=	Coefficient of Lift
C_M	=	Coefficient of Moment
C_μ	=	turbulence model constant, 0.09
D	=	low-Reynolds number term
E	=	total specific energy
E_ϵ	=	low-Reynolds number term
$f_{\epsilon 2}$	=	$1 - 0.3 \exp(-Re_t^2)$
f_μ	=	$\exp \left[\frac{-3.4}{(1+0.02Re_t)^2} \right]$
F, G, H	=	inviscid vector fluxes
F_v, G_v, H_v	=	viscous vector fluxes
J	=	Jacobian of coordinate trans- formation
k	=	turbulence kinetic energy
L_2	=	L_2 -norm of ΔQ
M_t	=	turbulence Mach number
M_∞	=	freestream Mach number
N_i, N_j, N_k	=	number of i, j, k grid points
p	=	nondimensional static pressure
p_t	=	nondimensional total pressure
P_k	=	turbulence production source term

Pr	=	Prandtl number, 0.73 for air
Pr_t	=	turbulent Prandtl number, 0.90
q_i	=	components of heat flux vector
Q	=	vector of dependent variables
R	=	gas constant
Re	=	reference Reynolds number, $\rho_\infty u_\infty c / \mu_\infty$
Re_t	=	turbulence Reynolds number, $Re(\rho k^2 / \mu \epsilon)$
s	=	distance along inclined wing upper surface
S	=	vector source term
t	=	nondimensional time
T	=	nondimensional static temperature
u, v, w	=	nondimensional Cartesian velocity components in x, y, z directions
u_1, u_2, u_3	=	u, v, w
U, V, W	=	contravariant velocity components
x, y, z	=	nondimensional Cartesian coordinates in streamwise, lateral, and vertical directions
x_1, x_2, x_3	=	x, y, z
γ	=	specific heat ratio, 1.4 for air
δ_{ij}	=	Kronecker delta function
ΔQ	=	variation in Q over Δt
Δt	=	time step size

ϵ	=	turbulence energy dissipation
μ, μ_t	=	molecular and turbulent viscosity coefficients
θ	=	angle of inclined wing upper surface
ξ, η, ζ	=	computational coordinates
$\xi_t, \xi_x, \xi_y, \xi_z,$ $\eta_t, \eta_x, \eta_y, \eta_z,$ $\zeta_t, \zeta_x, \zeta_y, \zeta_z$	=	metric coefficients of the coordinate transformation
ξ_1, ξ_2, ξ_3	=	ξ, η, ζ
ρ	=	nondimensional fluid density
σ	=	angle of incidence
σ_k	=	turbulence model constant, 1.0
σ_ϵ	=	turbulence model constant, 1.3
τ_{ij}	=	components of viscous stress tensor
<i>Subscripts</i>		
∞	=	freestream value

Acknowledgements

I am thankful for helpful discussions with members of CFD Research Section, Mr. M. J. Stanek, Drs. D. P. Rizzetta, R. E. Gordnier, D. Gaitonde, and M. R. Visbal. Help in using GRIDGEN3D by Capt. T. McClure of the Interdisciplinary & Applied CFD Section is gratefully acknowledged. Computational resources for this study was supported by a grant of HPC Shared Resource Centers, CEWES, Vicksburg, MS and NAVOCEANO, Bay St. Louis, MS.

1. Introduction

This work is part of a cooperative research, development, test and evaluation program that brings scientists and engineers from various English-speaking countries together for collaborative studies to improve technology to solve technical problems. The Technical Cooperation Program (TTCP) identified Computational Fluid Dynamics (CFD) as a critical technology. The current TTCP work project WTP-2 KTA 2-12, "Application of CFD to the prediction of Missile Body Vortices" extends on knowledge gained by KTA 2-9 and focuses on the ability of the three-dimensional Navier-Stokes equations to predict flowfields about high length-to-diameter bodies at moderate angles of attack ($8^\circ \leq \sigma \leq 14^\circ$) for transonic and supersonic Mach numbers.

This report documents this authors's computational results for the five test cases. The five test cases are as follows.

Case 1: Mach 1.45 at $\sigma = 14^\circ$, $Re_d = 616,666$.

Case 2: Mach 1.8 at $\sigma = 14^\circ$, $Re_D = 616,666$.

Case 3: Mach 2.5 at $\sigma = 14^\circ$, $Re_D = 1,233,333$.

Case 4: Mach 3.5 at $\sigma = 8^\circ$, $Re_D = 1,233,333$.

and Case 5: Mach 3.5 at $\sigma = 14^\circ$, $Re_D = 1,233,333$.

The experimental body is 13 diameters long with the diameter of the cylindrical afterbody of 3.7 inches. Laminar and turbulent computations are shown with comparisons to experimental data. The experimental validation data were provided by the Defence Research Agency (UK). The computations were performed with an existing Navier-Stokes code FDL3DI developed in the Wright Laboratory. The code features two kinds of spatial discretization which were used for the present studies, one having the central differences for both inviscid and viscous terms and the other having an upwind-biased discretization for the inviscid terms and the viscous terms are central differenced. The code includes the $k-\epsilon$ Turbulence model which was used for simulating turbulence effects in the flowfield. Grid resolution study was conducted to determine important areas in flow regimes where high grid densities are important to resolve the vortices and shocks and also for accurately predicting the surface pressure and pitot pressure in the flow field. In addition to the computation of five test cases on grids that were considered to be optimum for each of the cases, a standard grid was generated by members of the Wright Laboratory to be used by all the participants for comparing results with different CFD codes and turbulent models. The standard grid was computed only for Case 3 in the present study.

At supersonic Mach numbers the flowfields around missile body configurations at angle-of-attack have

boundary layer separation leading to vortical structures. The crossflow separation on the leeward side is characterized by the crossflow separation line and the strength of the vortex which develops from the separation. Prediction of these quantities by computational methods is highly dependent on the available turbulent models and their improvements.

There have been a number of numerical studies in recent years dealing with the problem of vortical flows for ogive-cylinder configurations at angle of attack [1, 2, 3, 4]. The importance of radial grid resolution for the attached turbulent viscous layers and the radial and circumferential resolution of the leeward vortices was noted by Degani, et al. [1]. Their work used the algebraic eddy-viscosity model and modifications were made to the turbulence model to properly evaluate the viscous-layer scale length under the leeward vortex structure. The computational work of Borrel et al. [2] also used the algebraic eddy-viscosity model and noted the problem of determining the mixing length where there were pronounced turbulent effects. The work of Hsieh, et al. [3] used the algebraic turbulence model modified by Degani, et al. [1] and found that the discrepancy between calculation and experiment increased at 10 and 15 degrees incidences for a three-inch diameter body at freestream Mach number of 3.5. The work of Moran, et al. [4] also used the algebraic turbulent model and made modifications to account for compressibility and pressure gradients and also altered the two coefficients in the outer region to better match the law of the wake. Computations were performed as a participant of the KTA 2-12 by Housh [5] using a TVD scheme and the Baldwin-Barth turbulence model.

In view of the importance of turbulence models in modeling these flows, the present work used the two-equation $k - \epsilon$ Turbulence model and compared it to the laminar solution results. The study contains numerical simulations of the Navier-Stokes equation with and without turbulent models for supersonic flows at moderate angles of attack for which detailed experimental data is available. Two different numerical spatial discretizations were used to compare solutions to determine if there were any issues pertaining to algorithm development.

The objectives of the current KTA 2-12 are to assess the current capabilities of Navier-Stokes solvers for the prediction of weapon flowfields and to promote technical interchange among CFD practitioners and experimental personnel in the areas of grid generation, solution algorithms, turbulence modeling, code performance, validation, and data visualization. The objectives will be accomplished by comparing the results obtained from Navier-Stokes computations against experimental data, evaluating the accuracy of the predictive technology and identifying priorities for future development.

2. Analysis

This section gives details of fluid dynamic equations and turbulence model of an existing computer code FDL3DI developed in the Wright Laboratory. The governing equations were taken to be the unsteady three-dimensional compressible mass-averaged turbulent Navier-Stokes equations, written in nondimensional variables and expressed notationally in the following strong-conservation form

$$\begin{aligned} \frac{\partial Q}{\partial t} + \frac{\partial}{\partial \xi} \left(F - \frac{1}{Re} F_v \right) + \frac{\partial}{\partial \eta} \left(G - \frac{1}{Re} G_v \right) \\ + \frac{\partial}{\partial \zeta} \left(H - \frac{1}{Re} H_v \right) + S = 0. \end{aligned} \quad (2.1)$$

Here t is the time, ξ, η, ζ the surface fitted computational coordinates, Q the vector of dependent variables, F, G, H the inviscid flux vectors, F_v, G_v, H_v the viscous flux vectors, and S the vector source term. Effects of turbulence were accounted for by specifying a turbulent Prandtl number $Pr_t = 0.90$, and by incorporating a two-equation model for the turbulence kinetic energy k and the turbulence dissipation rate ϵ . The $k - \epsilon$ turbulence model is that of Jones and Launder [6, 7] for which the generalized formulation was written by Gerolymos [8]. The model incorporates low Reynolds number terms to account for near-wall effects. The turbulence model is implemented with compressibility correction of Sarkar, et al. [9] for more accurate representation of supersonic flows.

With this formulation, the vector of dependent variables is given as

$$Q = \frac{1}{J} \begin{bmatrix} \rho \\ \rho u \\ \rho v \\ \rho w \\ \rho E \\ \rho k \\ \rho \epsilon \end{bmatrix} \quad (2.2)$$

and the vector fluxes by

$$F = \frac{1}{J} \begin{bmatrix} \rho U \\ \rho uU + \xi_x p \\ \rho vU + \xi_y p \\ \rho wU + \xi_z p \\ \rho EU + \xi_{x_i} u_i p \\ \rho kU \\ \rho \epsilon U \end{bmatrix} \quad (2.3)$$

$$G = \frac{1}{J} \begin{bmatrix} \rho V \\ \rho uV + \eta_x p \\ \rho vV + \eta_y p \\ \rho wV + \eta_z p \\ \rho EV + \eta_{x_i} u_i p \\ \rho kV \\ \rho \epsilon V \end{bmatrix} \quad (2.4)$$

$$H = \frac{1}{J} \begin{bmatrix} \rho W \\ \rho uW + \zeta_x p \\ \rho vW + \zeta_y p \\ \rho wW + \zeta_z p \\ \rho EW + \zeta_{x_i} u_i p \\ \rho kW \\ \rho \epsilon W \end{bmatrix} \quad (2.5)$$

$$F_v = \frac{1}{J} \begin{bmatrix} 0 \\ \xi_{x_i} \tau_{i1} \\ \xi_{x_i} \tau_{i2} \\ \xi_{x_i} \tau_{i3} \\ \xi_{x_i} (u_j \tau_{ij} - q_i) \\ (\mu + \mu_t / \sigma_k) \xi_{x_i} \frac{\partial \xi_j}{\partial x_i} \frac{\partial k}{\partial \xi_j} \\ (\mu + \mu_t / \sigma_\epsilon) \xi_{x_i} \frac{\partial \xi_j}{\partial x_i} \frac{\partial \epsilon}{\partial \xi_j} \end{bmatrix} \quad (2.6)$$

$$G_v = \frac{1}{J} \begin{bmatrix} 0 \\ \eta_{x_i} \tau_{i1} \\ \eta_{x_i} \tau_{i2} \\ \eta_{x_i} \tau_{i3} \\ \eta_{x_i} (u_j \tau_{ij} - q_i) \\ (\mu + \mu_t / \sigma_k) \eta_{x_i} \frac{\partial \xi_j}{\partial x_i} \frac{\partial k}{\partial \xi_j} \\ (\mu + \mu_t / \sigma_\epsilon) \eta_{x_i} \frac{\partial \xi_j}{\partial x_i} \frac{\partial \epsilon}{\partial \xi_j} \end{bmatrix} \quad (2.7)$$

$$H_v = \frac{1}{J} \begin{bmatrix} 0 \\ \zeta_{x_i} \tau_{i1} \\ \zeta_{x_i} \tau_{i2} \\ \zeta_{x_i} \tau_{i3} \\ \zeta_{x_i} (u_j \tau_{ij} - q_i) \\ (\mu + \mu_t / \sigma_k) \zeta_{x_i} \frac{\partial \xi_j}{\partial x_i} \frac{\partial k}{\partial \xi_j} \\ (\mu + \mu_t / \sigma_\epsilon) \zeta_{x_i} \frac{\partial \xi_j}{\partial x_i} \frac{\partial \epsilon}{\partial \xi_j} \end{bmatrix} \quad (2.8)$$

with the vector source term

$$S = \frac{1}{J} \begin{bmatrix} 0 \\ 0 \\ 0 \\ 0 \\ 0 \\ -[P_k - \rho \epsilon (1 + M_t^2) + D] \\ -(C_{\epsilon 1} P_k \epsilon / k - C_{\epsilon 2} f_{\epsilon 2} \rho \epsilon^2 / k + E_\epsilon) \end{bmatrix} \quad (2.9)$$

where

$$U = \xi_t + \xi_{x_i} u_i \quad (2.10)$$

$$V = \eta_t + \eta_{x_i} u_i \quad (2.11)$$

$$W = \zeta_t + \zeta_{x_i} u_i \quad (2.12)$$

$$E = \frac{T}{(\gamma - 1) M_\infty^2} + \frac{1}{2} (u^2 + v^2 + w^2). \quad (2.13)$$

In the preceding expressions, u, v, w are the Cartesian velocity components, ρ the density, p the pressure, and T the temperature. All length scales have been nondimensionalized by the diameter of the cylindrical afterbody D and dependent variables have been normalized by freestream values except for p, k , and ϵ

which have been nondimensionalized by $\rho_\infty u_\infty^2$, u_∞^2 , and u_∞^3/d respectively. Components of the heat flux vector and stress tensor may be expressed as

$$q_i = - \left[\frac{1}{(\gamma - 1)M_\infty^2} \right] \left(\frac{\mu}{Pr} + \frac{\mu_t}{Pr_t} \right) \frac{\partial \xi_j}{\partial x_i} \frac{\partial T}{\partial \xi_j} \quad (2.14)$$

$$\tau_{ij} = (\mu + \mu_t) \left(\frac{\partial \xi_k}{\partial x_j} \frac{\partial u_i}{\partial \xi_k} + \frac{\partial \xi_k}{\partial x_i} \frac{\partial u_j}{\partial \xi_k} - \frac{2}{3} \delta_{ij} \frac{\partial \xi_l}{\partial x_k} \frac{\partial u_k}{\partial \xi_l} \right) \quad (2.15)$$

and the turbulence parameters are

$$P_k = \frac{1}{Re} \tau_{ij} \frac{\partial \xi_k}{\partial x_j} \frac{\partial u_i}{\partial \xi_k} \quad (2.16)$$

$$\tau_{ij} = \mu_t \left(\frac{\partial \xi_k}{\partial x_j} \frac{\partial u_i}{\partial \xi_k} + \frac{\partial \xi_k}{\partial x_i} \frac{\partial u_j}{\partial \xi_k} - \frac{2}{3} \delta_{ij} \frac{\partial \xi_l}{\partial x_k} \frac{\partial u_k}{\partial \xi_l} \right) \quad (2.17)$$

$$M_t^2 = 2M_\infty^2 k/T \quad (2.18)$$

$$D = - \frac{2\mu}{Re} \sum_i \left(\frac{\partial \xi_j}{\partial x_i} \frac{\partial k^{1/2}}{\partial \xi_j} \right)^2 \quad (2.19)$$

$$E_\epsilon = \frac{2\mu\mu_t}{\rho Re^2} \sum_i \left(\frac{\partial \xi_k}{\partial x_j} \frac{\partial \xi_l}{\partial x_j} \frac{\partial^2 u_i}{\partial \xi_k \partial \xi_l} \right)^2 \quad (2.20)$$

$$Re_t = Re \left(\frac{\rho k^2}{\mu \epsilon} \right) \quad (2.21)$$

$$\mu_t = C_\mu f_\mu Re_t \mu \quad (2.22)$$

$$f_\mu = \exp \left[\frac{-3.4}{(1 + 0.02 Re_t)^2} \right] \quad (2.23)$$

$$f_{\epsilon 2} = 1 - 0.3 \exp(-Re_t^2) \quad (2.24)$$

$$C_\mu = 0.09, C_{\epsilon 1} = 1.44, C_{\epsilon 2} = 1.92 \quad (2.25)$$

$$\sigma_k = 1.0, \sigma_\epsilon = 1.3. \quad (2.26)$$

The Sutherland law for the molecular viscosity coefficient μ and the perfect gas relationship

$$p = \frac{\rho T}{\gamma M_\infty^2} \quad (2.27)$$

were also employed, and Stokes' hypothesis for the bulk viscosity coefficient has been invoked.

The coefficients of the force components given by the experiment are the C_x and C_z which are defined as follows:

$$C_{force} = \frac{Force}{0.5 \rho_\infty V_\infty^2 A} \quad (2.28)$$

The coefficient of moment is defined as follows:

$$C_{moment} = \frac{Moment}{0.5\rho_{\infty} V_{\infty}^2 AD} \quad (2.29)$$

The moments are measured about the nose tip ($X = 0$).

The coefficients of lift and drag are defined by:

$$C_L = C_z \cos \sigma - C_x \sin \sigma \quad (2.30)$$

$$C_D = C_z \sin \sigma + C_x \cos \sigma \quad (2.31)$$

In the above, the reference length D is the diameter of the body which is 3.7 in and the Area A is given by $\frac{\pi D^2}{4}$

Except for the axial force C_x , all the other comparisons are got by integrating the pressures and shear stresses on the body. The axial force experimental results are disturbed by the sting mounting and in the computation the freestream static pressure is applied over the base area.

The components of the stress tensor written in the non-dimensional variables is given by,

$$\tau_{xx} = -p + \frac{1}{Re}(\mu + \mu_t) \left[\frac{4}{3} \frac{\partial u}{\partial x} - \frac{2}{3} \left(\frac{\partial v}{\partial y} + \frac{\partial w}{\partial z} \right) \right] \quad (2.32)$$

$$\tau_{yy} = -p + \frac{1}{Re}(\mu + \mu_t) \left[\frac{4}{3} \frac{\partial v}{\partial y} - \frac{2}{3} \left(\frac{\partial u}{\partial x} + \frac{\partial w}{\partial z} \right) \right] \quad (2.33)$$

$$\tau_{zz} = -p + \frac{1}{Re}(\mu + \mu_t) \left[\frac{4}{3} \frac{\partial w}{\partial z} - \frac{2}{3} \left(\frac{\partial u}{\partial x} + \frac{\partial v}{\partial y} \right) \right] \quad (2.34)$$

$$\tau_{xy} = \tau_{yx} = \frac{1}{Re}(\mu + \mu_t) \left(\frac{\partial u}{\partial y} + \frac{\partial v}{\partial x} \right) \quad (2.35)$$

$$\tau_{xz} = \tau_{zx} = \frac{1}{Re}(\mu + \mu_t) \left(\frac{\partial u}{\partial z} + \frac{\partial w}{\partial x} \right) \quad (2.36)$$

$$\tau_{yz} = \tau_{zy} = \frac{1}{Re}(\mu + \mu_t) \left(\frac{\partial v}{\partial z} + \frac{\partial w}{\partial y} \right) \quad (2.37)$$

The components of force in the transformed coordinates are given by,

$$F_x = \int \int \frac{1}{|J|} (\eta_x \tau_{xx} + \eta_y \tau_{yx} + \eta_z \tau_{zx}) d\xi d\zeta \quad (2.38)$$

$$F_y = \int \int \frac{1}{|J|} (\eta_x \tau_{xy} + \eta_y \tau_{yy} + \eta_z \tau_{zy}) d\xi d\zeta \quad (2.39)$$

$$F_z = \int \int \frac{1}{|J|} (\eta_x \tau_{xz} + \eta_y \tau_{yz} + \eta_z \tau_{zz}) d\xi d\zeta \quad (2.40)$$

The mass averaged Navier-Stokes equations were solved using two kinds of spatial discretization both based on the implicit Beam and Warming algorithm. The central difference version implemented into the code is 2nd order accurate spatially and uses a blended 2nd/4th order Jameson-type damping. The other kind of spatial discretization which used the Roe Approximate Riemann solver for the inviscid terms which has 3rd order spatial accuracy and central differences for the viscous terms. The Navier-Stokes equations solved by the Beam and Warming algorithm were used successfully in analyzing vortex breakdown above a pitching delta wing by Visbal [10] and turbulent cylinder juncture flows by Rizzetta [11]. The Roe solver was used to study the turbulent interactions due to cylinder/offset flare juncture by Gaitonde, et al. [12].

2.1 Boundary Conditions

Since supersonic conditions were at both inflow and outflow, at the inflow, supersonic conditions were applied and at outflow extrapolation condition was used. Along the farfield boundary, freestream conditions were given. For the body surfaces, no slip was applied, zero normal pressure gradient and an adiabatic wall was used. For the turbulent case, homogeneous conditions for k and ϵ were specified.

A line of singularity in the coordinate transformation lies along the longitudinal axis and extends from the tip of the ogive to the upstream farfield boundary. The flow variables along this line ($i=1$) were simply set equal to the average of the flow variables on the $i=2$ surface. The flow is assumed to have bilateral symmetry with respect to the x - y plane; therefore $w=0$ and $\frac{\partial}{\partial \zeta} = 0$ for all the remaining variables.

2.2 Experimental Data and Conditions of Numerical Simulation

The experimental data were provided by the Defence Research Agency, UK. The geometry consists of a length of 13 diameters as shown in Figure 1. The nose is given by the equation:

$$r(x)/D = -0.002615(x/D)^3 - 0.03986(x/D)^2 + 0.30984(x/D) \quad (2.41)$$

Fig. 2 shows the body and the computational grid used for computing the conditions of Case 1. For this case, the asymmetry in the grid allows for better capture of vortices on the leeward side and the strong shock close to the body on the windward side. The grid was generated using the GRIDGEN3D [13].

The five test cases chosen for this study are the free stream conditions shown in the Table 2.1. Prioritization of the cases as determined by the TTCP workgroup is shown in Table 2.1.

Table 2.1: Free Stream Conditions

Case No.	Priority No.	Mach No.	Angle of Attack, deg.	Re_D	Total press., N/m^2	Total temp., K
1	5	1.45	14	616,666	44,912	301
2	2	1.8	14	616,666	47,276	304
3	1	2.5	14	1,233,333	141,827	308
4	3	3.5	8	1,233,333	243,133	315
5	4	3.5	14	1,233,333	243,133	315

Table 2.2: Available Experimental Data

Case No.	Surface Pressure, C_p	Pitot Pressure
1	$X/D=0.2-14.5, \phi=0-180$	$X/D=8.5$ and 11.5
2	$X/D=0.2-14.5, \phi=0-180$	$X/D=5.5, 8.5$ and 11.5
3	$X/D=0.2-14.5, \phi=0-180$	$X/D=8.5$ and 11.5
4	$X/D=0.2-14.5, \phi=0-180$	$X/D=5.5$
5	$X/D=0.2-14.5, \phi=0-180$	$X/D=5.5$ and 11.5

The experimental data consist of surface pressure and pitot pressure. The surface pressure is at 32 axial locations and the pitot pressure is at axial locations as specified in the Table 2.2. Although, the computations were performed for a length of 13 diameters, the experimental body was longer and the pressure coefficients were taken upto a length of 14.5 diameters.

The grids developed for this study are of the C-type grids. Since the study was pertaining to steady state solutions, only a half grid in the circumferential direction was used. Except for the grid for Case 1 and the standard grid, the C-grid was rotated about the longitudinal axis for the body to construct the three-dimensional grid. For the grid for Case 1 and the standard grid, the GRIDGEN3D [13] was used to rotate the grid about the longitudinal axis for an asymmetry required for better resolution of vortical structures on the leeward side and the shock wave close to the body on the windward side.

The feature of local time stepping was used for the central difference version of the code to speed up convergence to steady state. The constant nondimensional time steps employed for these calculations, as dictated by stability requirements are $0.01 \leq \sigma \leq 0.0001$. The turbulent calculation was started from the

Table 2.3: Details of grids considered in this study

Case No.	Mach No.	AoA	Re_d	Δ_n	Grid size
1	1.45	14°	616,666	0.00001	173 x 99 x 93
2	1.8	14°	616,666	0.00003	150 x 82 x 75
3	2.5	14°	1,233,333	0.00003	100 x 50 x 51
3	2.5	14°	1,233,333	0.00003	150 x 75 x 76
3	2.5	14°	1,233,333	0.00001	121 x 89 x 89
4	3.5	8°	1,233,333	0.00003	150 x 75 x 76
5	3.5	14°	1,233,333	0.00003	150 x 75 x 76

Δ_n = Minimum Normal Grid Spacing normalized by $R_n = 3.7in$

Grid size is given as: axial x radial x circumferential

converged laminar solution.

2.3 Grid Study

A grid study was conducted to determine the optimum grid required to compare the computational results to data. The grid study results are shown only for Case 3. The grid sizes and minimum distances for all three grids for Case 3 and for the other cases is given in Table 2.3. The laminar and turbulent pitot pressure along the vortex centerline for the three grids for Case 3 is shown at an X/D location of 11.5 in Figures 3 and 4. It can be seen that as the points in the radial and circumferential direction are increased, the vortex shape is better captured. The surface pressure, however, for all three grids have small variations with each other (figures not shown). From the comparison of laminar and turbulent computations it can also be seen that the vortex core is better captured in the turbulent case.

3. Computer Requirements

The computational resources used for computing the test cases employing three different grids used in the present study are summarized in this section. The summary shown in Table 3.1 gives the computer resources used for computational results presented in this report.

The Data Processing Rate (DPR) for the laminar cases for both Central and Upwind difference versions are close to each other. The DPR for the turbulent cases are significantly higher due to the inclusion of the two-equation $k-\epsilon$ turbulence model. Part of the reason for the high DPR is because the computer code for the turbulence model is not fully optimized.

The Cray C-90 was used for computation of all test cases

Table 3.1: Computer resources requirements

Grid Size	Type of discretization	Laminar or Turbulent	DPR	Memory
100 x 50 x 51	Central	Laminar	2.3	10 Mw
100 x 50 x 51	Central	Turbulent	5.4	10 Mw
150 x 75 x 76	Central	Laminar	7.7	33 Mw
150 x 75 x 76	Central	Turbulent	18.0	33 Mw
121 x 89 x 89	Central	Laminar	8.3	37 Mw
121 x 89 x 89	Central	Turbulent	20.2	37 Mw
121 x 89 x 89	Upwind	Laminar	11.3	37 Mw
121 x 89 x 89	Upwind	Turbulent	24.5	37 Mw

DPR = Data Processing Rate

Grid size is given as: axial x radial x circumferential

4. Discussion of Results

This section has discussion of results for computations of all five test cases and the computations on the standard grid for the Case 3. The computations on the standard grid use the two types of spatial discretization - (a) central differences for inviscid and viscous terms and (b) upwind differences for inviscid terms.

4.1 Surface Pressure Comparisons for Case 3 on Standard Grid

Figures 5- 20 show the computed surface pressure comparisons with experiments. The comparisons are for both versions of the code, namely central and upwind difference and for both laminar and turbulent computations. The results are shown for various axial stations of $X/D = 2.4, 3.5, 4.5, 5.5, 6.5, 7.5, 8.5,$ and 11.5 . For all the results shown, the surface pressures obtained by central difference and upwind difference are very close to each other. The laminar and turbulent computations, however, are showing differences after ϕ of 90° for all stations, the variation becoming greater as X/D increases. The comparison of turbulent computations agree with the experiment better than the laminar computations at all X/D locations. The laminar computations show additional suction peaks beyond ϕ of 60° for all locations denoting additional vortical structures in the flow field. The turbulent computation underpredicts the second suction peak at X/D of $4.5, 5.5,$ and 8.5 (shown in Figures 10, 11, and 18) which can be attributed to excess dissipation of the $k-\epsilon$ Turbulence model. The surface pressure beyond 120° at X/D of 8.5 shown in Figure 18 shows poor comparison with experimental values. The surface pressure comparisons between the central difference and the upwind difference versions show very little variations for both laminar and turbulent computations.

4.2 Pitot Pressure Comparisons for Case 3 on Standard Grid

The pitot pressure contours predicted by computations and the pressure extracted along the vortex centerline are compared to the pitot pressure contours and pressure extracted along the vortex centerline of the experiment in Figures 21 to 32. The computational results shown are for both laminar and turbulent for the central and upwind difference versions on the standard grid. The pitot pressure of the computation outside of the vortex is same as the experiment. The shock wave at an angle of about 45° of the circular cross-section for the experimental pitot pressure contours is better captured for the turbulent case than for the laminar, as can be seen in Figures 21 and 22. The pitot pressure along the vortex centerline shows the

turbulent computations to be better than laminar shown in Figures 23 and 26; however, at X/D of 11.5, the vortex pressure of the laminar case matches the experimental value better, as seen in Figures 29 and 32. For the laminar computation, additional vortices can be seen at X/D of 11.5 as seen in Figure 27 and 30.

4.3 Pitot Pressure Comparisons for Cases 1 to 5

The pitot pressure comparisons and pressure along vortex centerline for Case 1 are shown in Figures 33 to 38. Additional suction peaks are seen in the turbulent computations at X/D of 8.5 and 11.5 as seen in Figures 35 and 38. At X/D of 11.5 the vortex shows excessive dissipation due to the effects of the turbulence model as seen in Figures 37 and 38.

The pitot pressure comparisons and pressure along vortex centerline for Case 2 are given in Figures 39 to 46. There is no well-defined vortex in the computation at X/D location of 5.5, hence no comparison is made for pressure along vortex centerline with experiment. At X/D of 8.5, the laminar computation compares with experiment better than the turbulent case as can be clearly seen from the comparison of pressures along the vortex centerline. At X/D of 11.5, both laminar and turbulent pitot pressures show the vortex to be more dissipated than the vortex in experiment. However, the shape and size of the laminar vortex compares well with the experiment. The pitot pressure comparisons for Case 3 are shown in Figures 47 to 51. There is no clear vortex center in the computation at X/D of 5.5 hence, no pitot pressure along vortex centerline is shown in comparison to experiment. At X/D of 11.5, the comparison between the laminar and turbulent computations and experiment are reasonable with the vortex-core of the laminar computation matching the experiment better than the turbulent case. The pitot pressure comparisons and the pressure along the vortex centerline for Case 4 are shown in Figures 52 to 54. The vortex position shown in Figures 52, 53 and 54 is better predicted for the turbulent case than for the laminar case; however, the turbulent model causes excess dissipation. The pitot pressure comparisons and the pressure along vortex centerline for Case 5 are shown in Figures 55 to 59. The comparison between the experiment and computation at X/D of 5.5 is reasonable as shown in Figures 55 and 56. At X/D of 11.5, referring to Figures 57 and 58 the pitot pressure contours of the computations do not show the details of the vortex structure as seen in the experiment. The vortex centerline pressure, however, shows reasonable comparison with experiment.

4.4 Surface Pressure Comparisons for Cases 1 to 5

The surface pressure comparisons for Case 1 are shown in Figures 60 to 67. The surface pressure using the turbulence model shows better comparison than laminar. There are as many as four suction peaks showing in some laminar profiles. The profile using the turbulent model at X/D of 4.5, 5.5 and 6.5 shows the excess diffusivity of the turbulence model. The surface pressure comparisons for Case 2 are shown in Figures 68 to 75. The surface pressure using the turbulence model compares to the experiment very well at all the X/D locations shown. The suction peak has shifted compared to the experiment for the turbulence profile in the case of X/D of 6.5. The excess diffusivity of the turbulence model can be seen at X/D of 5.5, 6.5 and 7.5. The surface pressure comparisons for Case 3 are shown in Figures 76 to 83. The profiles using the turbulence model shows better comparison with experiment than the laminar. The most notable discrepancy of the turbulent profile with the experiment is at the X/D location of 7.5; after the suction peak at $\phi = 90^\circ$, the turbulent computation matches the laminar better than the experiment.

The surface pressure comparisons for Case 4 are shown in Figures 84 to 91. The turbulent computation profiles match the experiment very well. At X/D locations of 7.5 and 8.5, there is, however, excess dissipation due to the turbulence model which gives a higher suction pressure at $\phi = 150^\circ$. The surface pressure comparisons for Case 5 are shown in Figures 92 to 99. The turbulent profiles compare with the experiment better than the laminar ones. The turbulent profile at X/D of 6.5 matches the laminar profile better than the experiment.

4.5 Convergence History for Case 3 on Standard Grid

The convergence history of the solution using the upwind version of the code to reach steady state is shown in Figures 100 and 101. For the laminar case the $L2$ norm is reduced to six orders of magnitude and for the turbulent case convergence is assumed when the normalized surface pressure (averaged over the entire surface of the body) is shown to reach steady state.

4.6 Forces and Moments for Case 3 on Standard Grid

The axial and radial components of the force and the moment about y was computed for Case 3 using both the central and upwind difference versions of the code. The Table 4.1 gives the comparison of forces and moments for Case 3 on the standard grid.

Referring to Table 4.1, it can be seen that the predictions by turbulent computations made with both

Table 4.1: Comparison of Forces and Moments with Experiment for Central and Upwind Difference Versions for Case 3 on Standard Grid

	Exp.	Laminar (Central)	Turbulent (Central)	Laminar (Upwind)	Turbulent (Upwind)
-C _x (axial comp.)	0.1957	0.1281	0.1587	0.1313	0.1627
-C _z (radial comp.)	1.9100	2.0350	1.9127	1.9295	1.8146
C_L	1.8060	1.9434	1.8174	1.8404	1.7213
C_D	0.6520	0.6165	0.6167	0.4942	0.5969
C_M about y	-10.2417	-11.6243	-10.3066	-10.6691	-9.6580

Refer Figure 1 for sign convention

Experimental values are interpolated from data at σ of 12.16° and 14.20°

the central and upwind difference versions match the experimental C_x , C_z , C_L , C_D , and C_M better than the predictions by laminar computations.

5. Summary and Conclusions

As part of TTCP work project, the KTA 2-12 "Application of CFD to the prediction of missile body vortices," computations were performed to assess the predictive capability of full Navier-Stokes equations with turbulence model for two different types of discretization for the convective terms. An existing Navier-Stokes code FDL3DI developed in the Wright Laboratory was used to perform the computations. In the code the mass averaged Navier-Stokes equations were solved with the implicit Beam and Warming algorithm using (a) the central difference for both convective and viscous terms with the required numerical damping and (b) the upwind difference discretization for convective terms and central differences for viscous terms without explicit numerical damping. The turbulence model which is part of FDL3DI, chosen for this study was the $k-\epsilon$ Turbulence model. The turbulence model included compressibility correction and the low Reynolds number terms to include near-wall effects. All computational results were compared to the experimental data provided by the Defence Research Agency (DRA), UK.

The Cases 1-5 as classified and prioritized by TTCP workgroup were selected for the present study. The No. 1 priority case which is the Case 3 was selected for presenting the results of grid study. A standard grid was generated in the Wright Laboratory, USA, the purpose of which was to compare results from different CFD codes of all participants on one common grid. For the present study, the Case 3 was selected to run on the standard grid using both the Central and Upwind difference versions. All the Cases 1-5 were computed for the most optimum grid using the Central difference version only. Laminar and turbulent computations were compared to each other to delineate the effects of the turbulence model for all the cases selected.

Results are presented for surface pressure at several axial stations namely at X/D of 2.4, 3.5, 4.5, 5.5, 6.5, 7.5, 8.5 and 11.5. Pitot pressure comparisons in the flowfield are shown depending on the availability of experimental data at X/D locations of 5.5, 8.5, and 11.5. The axial and radial components of force and moment data predicted by the computational code for the standard grid of Case 3 was compared to the data obtained from experiments. Convergence histories for a laminar and turbulent computation as representative of computations performed to reach steady state in the present study, are shown in this report.

The important results of the study are summarized as follows. The surface pressure and pitot pressure comparisons show very little variation between the central and upwind difference versions for both laminar and turbulent computations. The surface pressure comparisons using the turbulence model have matched the experiment better than those with laminar computations. At an X/D location between 6.5 and 8.5 at

ϕ between 120° to 160° the surface pressure predicted by the turbulent computation matches the laminar computation and both do not match the experiment. From the pitot pressure comparisons and the matching of the vortex centerlines with experimental data we may make the following observations. The excessive dissipation in the turbulence model in the capturing of the vortices is evident from the comparisons of the shape of the vortices; for cases 1, 2, 3, 4 and 5 the laminar prediction of the vortex core centerline matches the experiment better than the turbulent prediction at select X/D locations. The pitot pressure comparisons show that the shock waves outside of the vortex is captured in the turbulent computations and not the laminar ones. Below the primary vortex there are two or three vortical structures for the laminar computations and none for the turbulent computations.

One of the main recommendations of this study is the development of better turbulence models to simulate vortical flow features. The inclusion of turbulence model has been shown to be important in the accurate prediction of surface pressure. The $k-\epsilon$ turbulence model has shown to be very dissipative in regions of vortices. This suggests that modifications of the model which distinguishes the regimes near wall and vortex. The other important area of development should be in the methodology to improve grid resolution locally such as embedded and adaptive grids to better capture the vortical structures. This will help to predict more accurately the strength and position of the vortical flows.

6. References

- [1] D. Degani and L.B. Schiff. Computation of Turbulent Supersonic Flows Around Pointed Bodies Having Crossflow Separation . *Journal of Computational Physics*, 66:173-196, 1986.
- [2] M. Borrel, P. d'Espiney, and C. Jouet. Supersonic Vortical Flows Around an Ogive-Cylinder. In *First European Computational Fluid Dynamics Conference*, Brussels, Belgium, September 1992.
- [3] T. Hsieh, F.J. Priolo, and A.B. Wardlaw, Jr. Calculations and Comparisons of the Flowfield About an Ogive Cylinder at $M=3.5$. *Journal of Spacecrafts and Rockets*, 30(6):665-673, 1993.
- [4] K.J. Moran and P.S. Beran. Navier-Stokes Simulations of Slender Axisymmetric Shapes in Supersonic, Turbulent Flow. *AIAA J*, 32(7):1446-1456, July 1994.
- [5] C.S. Housh. Comparison of Navier-Stokes Solutions and Experimental Flowfield and Surface Pressure Data for Slender Body Vortical Flow at Supersonic Mach Numbers and Moderate Angles of Attack. Technical Report NAWCWPNS TM 7709, Naval Air Warfare Center Weapons Division, China Lake, CA 93555-6001, March 1994.
- [6] W.P. Jones and B.E. Launder. The Prediction of Laminarization with a Two-Equation Model of Turbulence . *International Journal of Heat and Mass Transfer*, 15(2):301-314, 1972.
- [7] W.P. Jones and B.E. Launder. The Calculation of Low-Reynolds Number Phenomena with a Two-Equation Model of Turbulence . *International Journal of Heat and Mass Transfer*, 16(6):1119-1130, 1973.
- [8] G.A. Gerolymos. Implicit Multiple-Grid Solutions of the Compressible Navier-Stokes Equations Using $k - \epsilon$ Turbulence Closure. *AIAA J*, 28(10):1707-1717, 1990.
- [9] S. Sarkar, G. Erlebacher, M.Y. Hussaini, and H.O. Kreiss. The Analysis and Modelling of Dilatational Terms in Compressible Turbulence . *Journal of Fluid Mechanics*, 227:473-493, 1991.
- [10] M.R. Visbal. Onset of Vortex Breakdown Above a Pitching Delta Wing. *AIAA J*, 32(8):1568-1575, August 1994.
- [11] D.P. Rizzetta. Numerical Simulation of Turbulent Cylinder Juncture Flowfields . *AIAA Paper 93-3038*, 1993.

- [12] D. Gaitonde, J.R. Edwards, and J.S. Shang. The Computed Structure of a 3-D Turbulent Interaction Caused by a Cylinder/Offset Flare Junction. *AIAA Paper 95-0230*, 1995.
- [13] J.P. Steinbrenner, J.P. Chawner, and C.L. Fouts. The GRIDGEN 3D Multiple Block Grid Generation System, Volume II: User's Manual. Technical Report WRDC-TR-90-3022, FDL, WRDC, WPAFB, OH 45433-6553, February 1991.

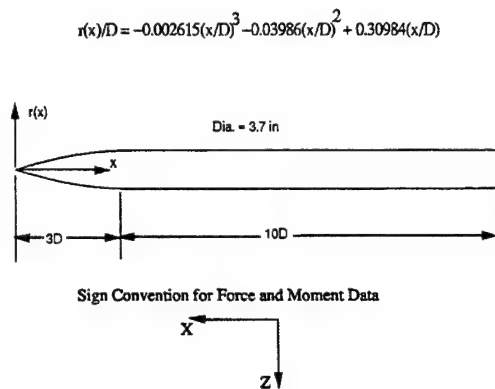
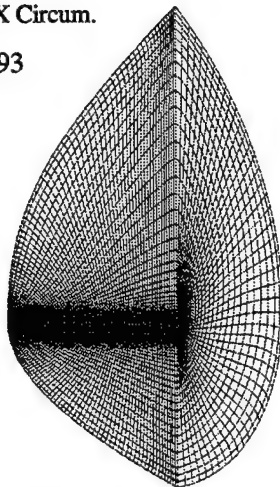


Figure 1: Experimental Data Geometry

Axial X Radial X Circum.
173 X 99 X 93



Grid Used for Case 1: Mach = 1.45 AoA = 14 deg.

Figure 2: Computational Grid

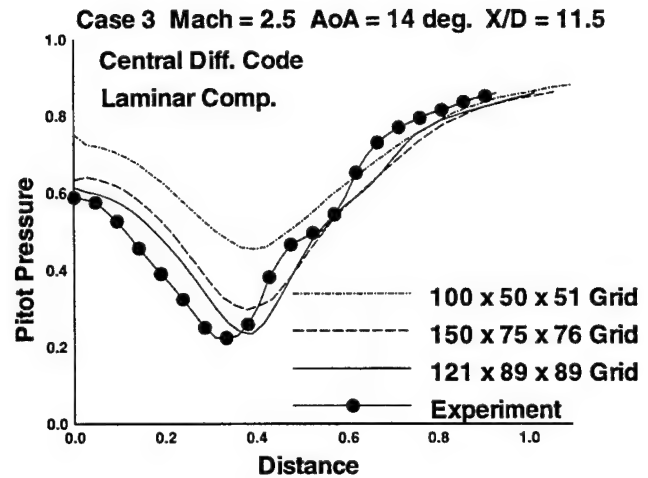


Figure 3: Grid Study: Comparison of Pitot Pressure along Vortex Centerline for Laminar

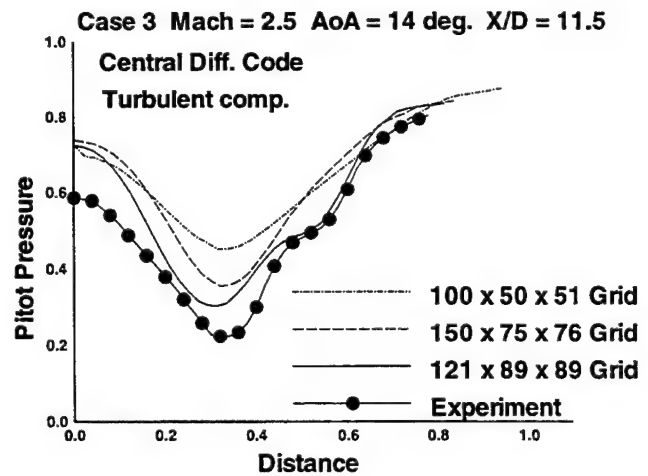


Figure 4: Grid Study: Comparison of Pitot Pressure along Vortex Centerline for Turbulent

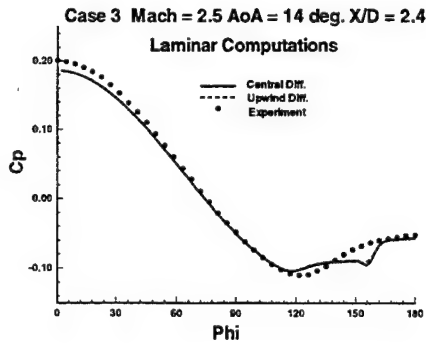


Figure 5: Comparison of Surface Pressure on Standard Grid at $X/D = 2.4$ for Laminar

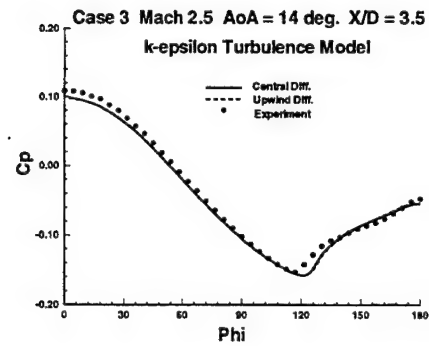


Figure 8: Comparison of Surface Pressure on Standard Grid at $X/D = 3.5$ for Turbulent

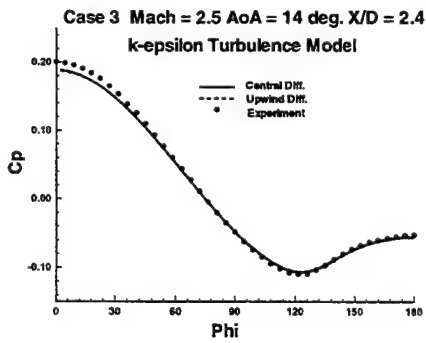


Figure 6: Comparison of Surface Pressure on Standard Grid at $X/D = 2.4$ for Turbulent

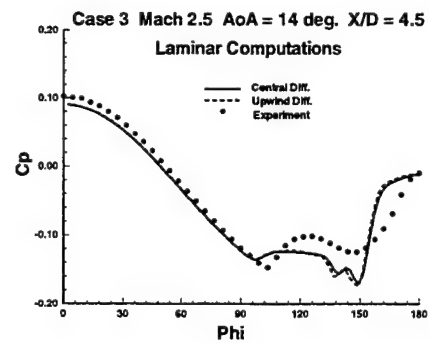


Figure 9: Comparison of Surface Pressure on Standard Grid $X/D = 4.5$ for Laminar

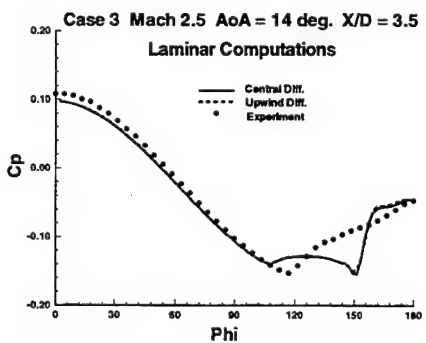


Figure 7: Comparison of Surface Pressure on Standard Grid at $X/D = 3.5$ for Laminar

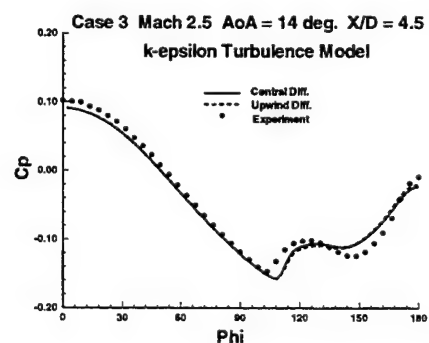


Figure 10: Comparison of Surface Pressure on Standard Grid $X/D = 4.5$ for Turbulent

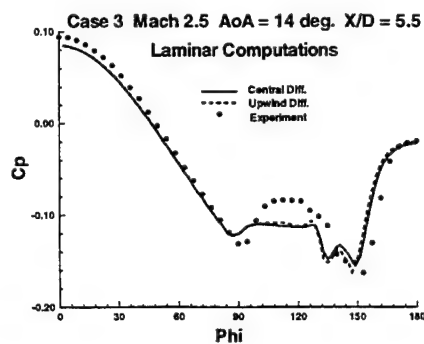


Figure 11: Comparison of Surface Pressure on Standard Grid at $X/D = 5.5$ for Laminar

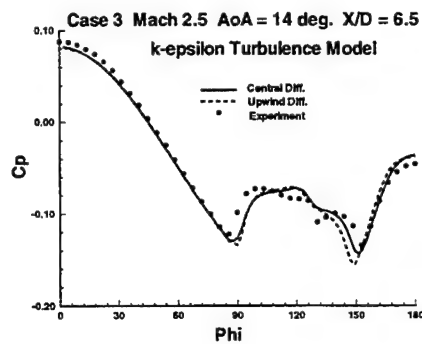


Figure 14: Comparison of Surface Pressure on Standard Grid at $X/D = 6.5$ for Turbulent

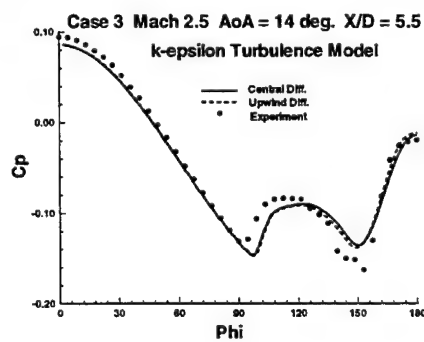


Figure 12: Comparison of Surface Pressure on Standard Grid at $X/D = 5.5$ for Turbulent

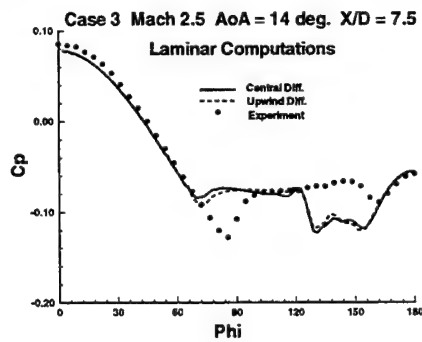


Figure 15: Comparison of Surface Pressure on Standard Grid at $X/D = 7.5$ for Laminar

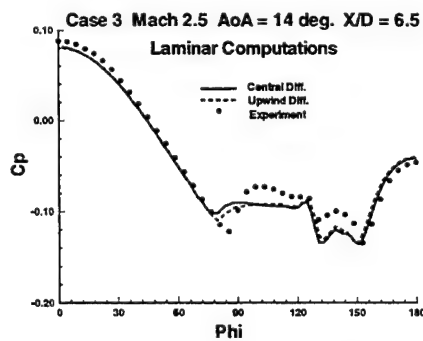


Figure 13: Comparison of Surface Pressure on Standard Grid at $X/D = 6.5$ for Laminar

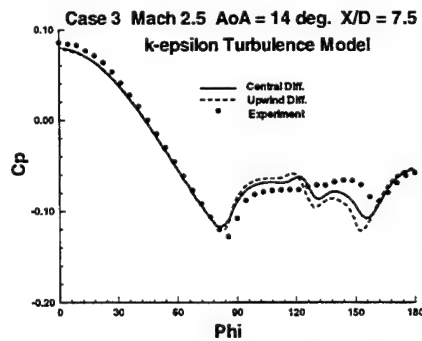


Figure 16: Comparison of Surface Pressure on Standard Grid at $X/D = 7.5$ for Turbulent

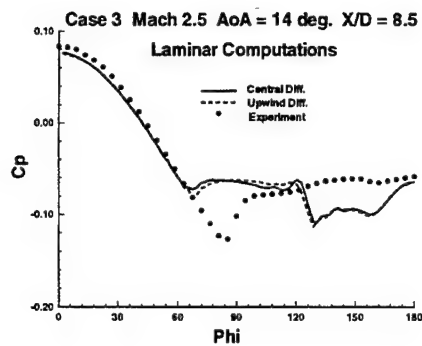


Figure 17: Comparison of Surface Pressure on Standard Grid at X/D = 8.5 for Laminar

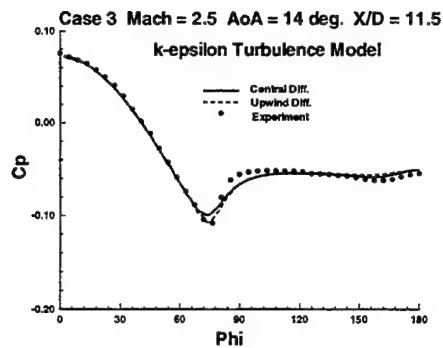


Figure 20: Comparison of Surface Pressure on Standard Grid at X/D = 11.5 for Turbulent

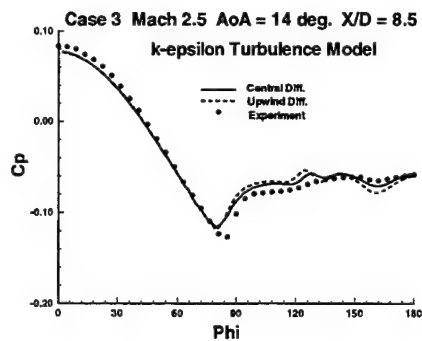


Figure 18: Comparison of Surface Pressure on Standard Grid at X/D = 8.5 for Turbulent

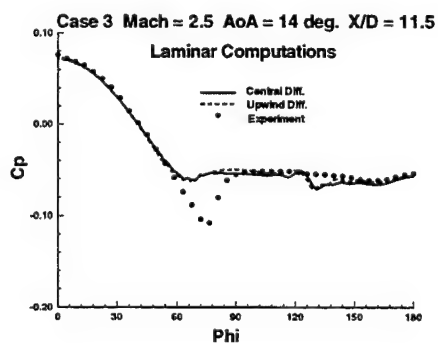


Figure 19: Comparison of Surface Pressure on Standard Grid at X/D = 11.5 for Laminar

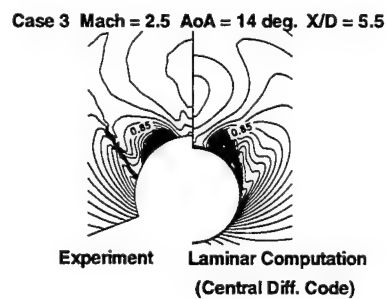


Figure 21: Comparison of Pitot Pressure on Standard Grid at X/D = 5.5 using Central Diff. (Laminar)

Case 3 Mach = 2.5 AoA = 14 deg. X/D = 5.5

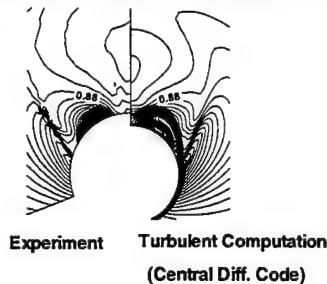


Figure 22: Comparison of Pitot Pressure on standard grid at $X/D = 5.5$ using Central Diff. (Turbulent)

Case 3 Mach = 2.5 AoA = 14 deg. X/D = 5.5

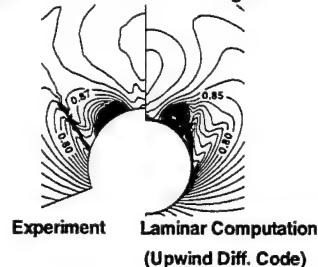


Figure 24: Comparison of Pitot Pressure on Standard Grid at $X/D = 5.5$ using Upwind Diff. (Laminar)

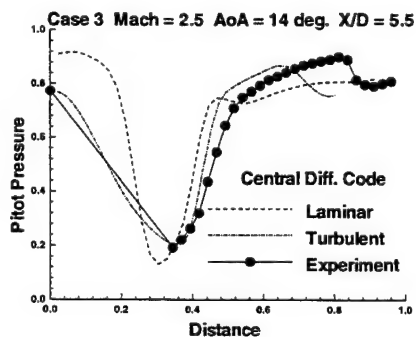


Figure 23: Comparison of Pitot Pressure along Vortex Centerline using Standard Grid at $X/D = 5.5$ using Central Diff.

Case 3 Mach = 2.5 AoA = 14 deg. X/D = 5.5

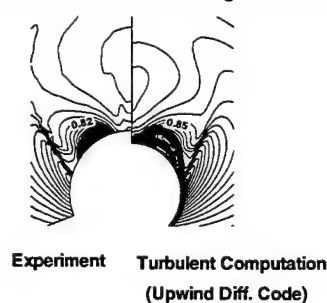


Figure 25: Comparison of Pitot Pressure on Standard Grid at $X/D = 5.5$ using Upwind Diff. (Turbulent)

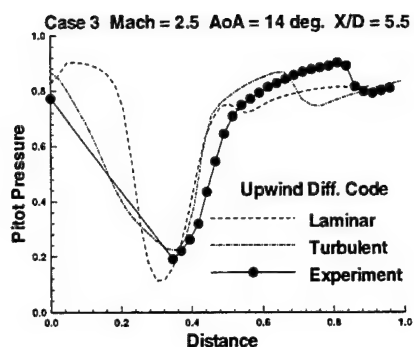


Figure 26: Comparison of Pitot Pressure along Vortex Centerline using Standard Grid at $X/D = 5.5$ using Upwind Diff.

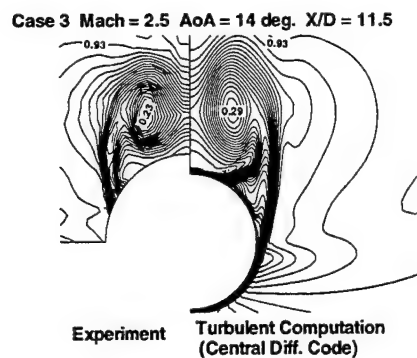


Figure 28: Comparison of Pitot Pressure on Standard Grid at $X/D = 11.5$ using Central Diff. (Turbulent)

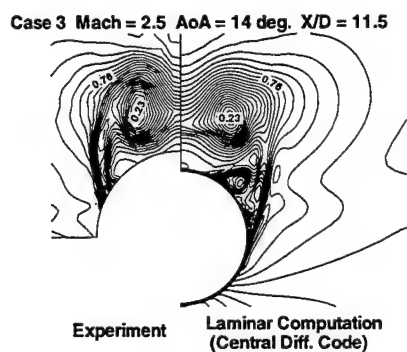


Figure 27: Comparison of Pitot Pressure on Standard Grid at $X/D = 11.5$ using Central Diff. (Laminar)

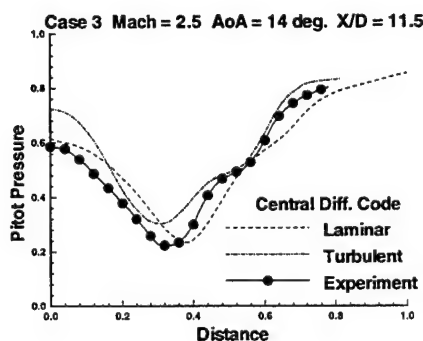


Figure 29: Comparison of Pitot Pressure along Vortex Centerline using Standard Grid at $X/D = 11.5$ using Central Diff.

Case 3 Mach = 2.5 AoA = 14 deg. X/D = 11.5

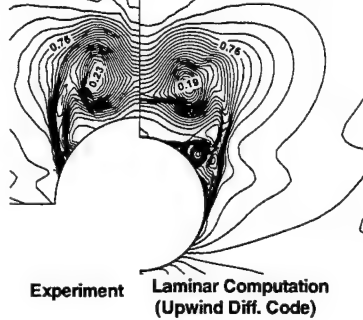


Figure 30: Comparison of Pitot Pressure on Standard Grid at X/D = 11.5 using Upwind Diff. (Laminar)

Case 3 Mach = 2.5 AoA = 14 deg. X/D = 11.5

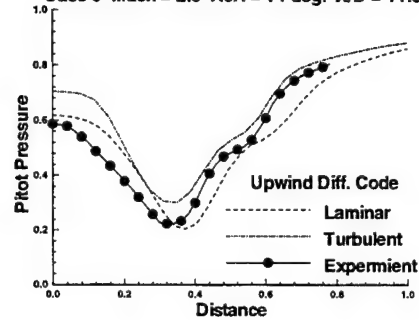


Figure 32: Comparison of Pitot Pressure along Vortex Centerline using Standard Grid at X/D = 11.5 using Upwind Diff.

Case 3 Mach = 2.5 AoA = 14 deg. X/D = 11.5

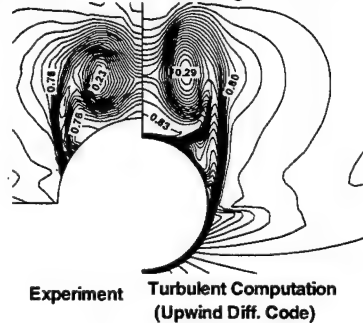


Figure 31: Comparison of Pitot Pressure on Standard Grid at X/D = 11.5 using Upwind Diff. (Turbulent)

Case 1 Mach = 1.45 AoA = 14 deg. X/D = 8.5

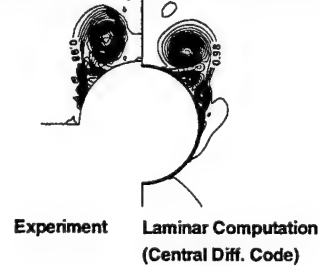


Figure 33: Comparison of Pitot Pressure for Case 1 at X/D = 8.5 (Laminar)

Case 1 Mach = 1.45 AoA = 14 deg. X/D = 8.5

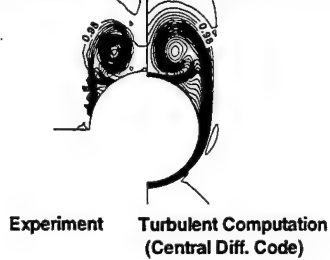


Figure 34: Comparison of Pitot Pressure for Case 1 at X/D = 8.5 (Turbulent)

Case 1 Mach = 1.45 AoA = 14 deg. X/D = 11.5

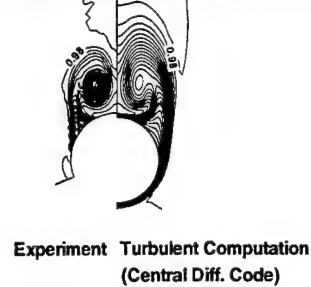


Figure 37: Comparison of Pitot Pressure for Case 1 at X/D = 11.5 (Turbulent)

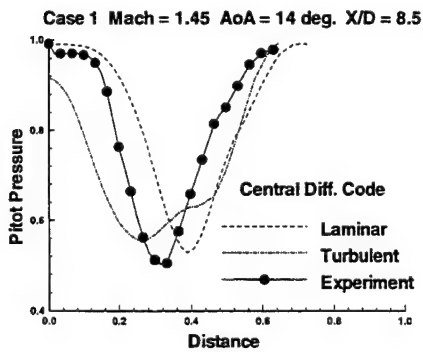


Figure 35: Comparison of Pitot Pressure along Vortex Centerline for Case 1 at X/D = 8.5

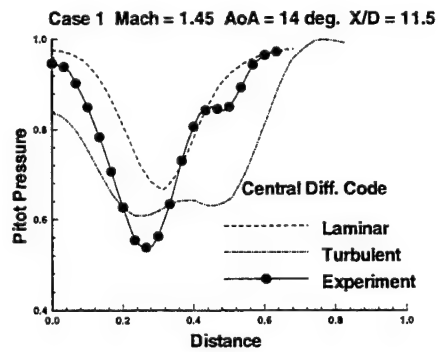


Figure 38: Comparison of Pitot Pressure along Vortex Centerline for Case 1 at X/D = 11.5

Case 1 Mach = 1.45 AoA = 14 deg. X/D = 11.5

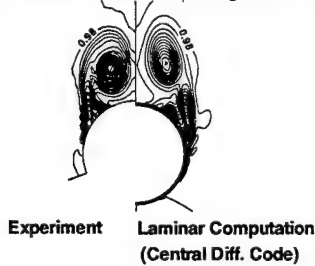


Figure 36: Comparison of Pitot Pressure for Case 1 at X/D = 11.5 (Laminar)

Case 2 Mach = 1.8 AoA = 14 deg. X/D = 5.5

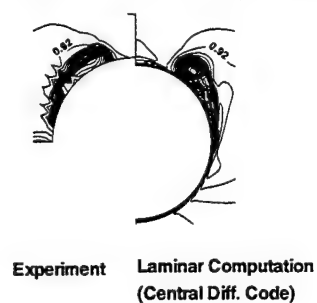


Figure 39: Comparison of Pitot Pressure for Case 2 at X/D = 5.5 (Laminar)

Case 2 Mach = 1.8 AoA = 14 deg. X/D = 5.5

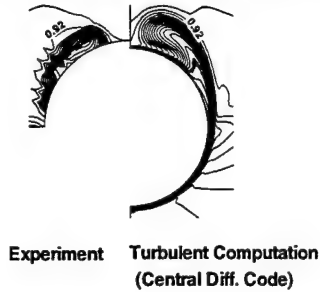


Figure 40: Comparison of Pitot Pressure for Case 2 at X/D = 5.5 (Turbulent)

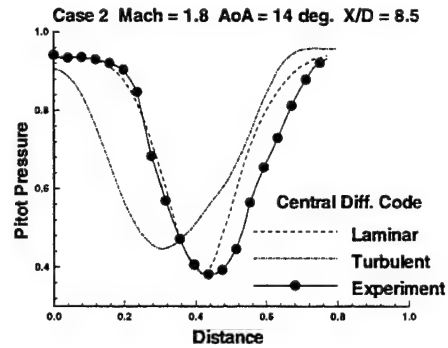


Figure 43: Comparison of Pitot Pressure along Vortex Centerline for Case 2 at X/D = 8.5

Case 2 Mach = 1.8 AoA = 14 deg. X/D = 8.5

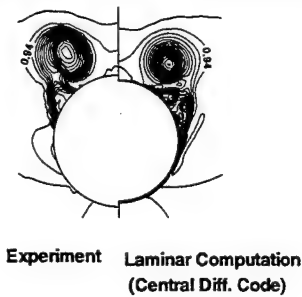


Figure 41: Comparison of Pitot Pressure for Case 2 at X/D = 8.5 (Laminar)

Case 2 Mach = 1.8 AoA = 14 deg. X/D = 11.5

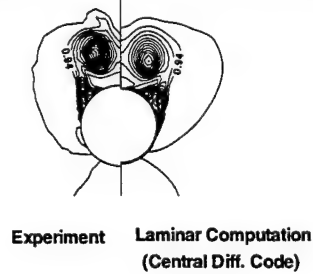


Figure 44: Comparison of Pitot Pressure for Case 2 at X/D = 11.5 (Laminar)

Case 2 Mach = 1.8 AoA = 14 deg. X/D = 8.5

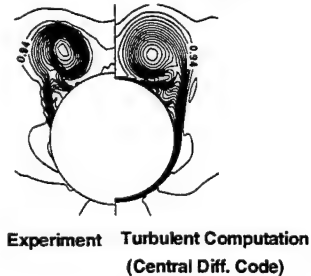


Figure 42: Comparison of Pitot Pressure for Case 2 at X/D = 8.5 (Turbulent)

Case 2 Mach = 1.8 AoA = 14 deg. X/D = 11.5

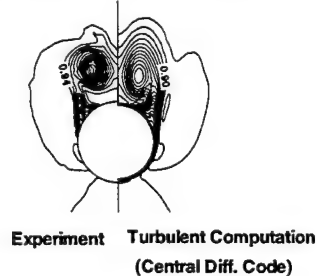


Figure 45: Comparison of Pitot Pressure for Case 2 at X/D = 11.5 (Turbulent)

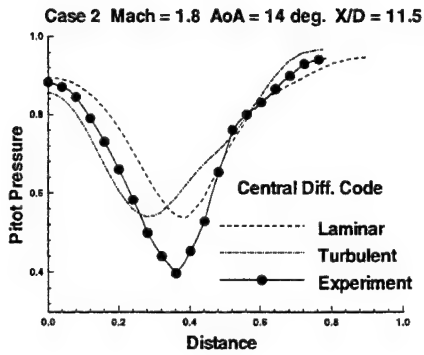


Figure 46: Comparison of Pitot Pressure along Vortex Centerline for Case 2 at $X/D = 11.5$

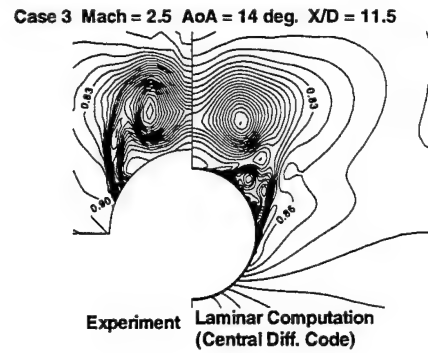


Figure 49: Comparison of Pitot Pressure for Case 3 at $X/D = 11.5$ (Laminar)

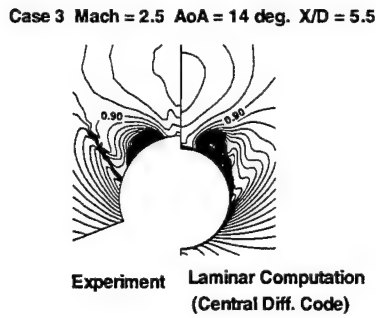


Figure 47: Comparison of Pitot Pressure for Case 3 at $X/D = 5.5$ (Laminar)

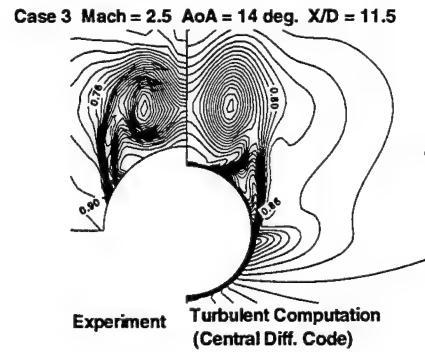


Figure 50: Comparison of Pitot Pressure for Case 3 at $X/D = 11.5$ (Turbulent)

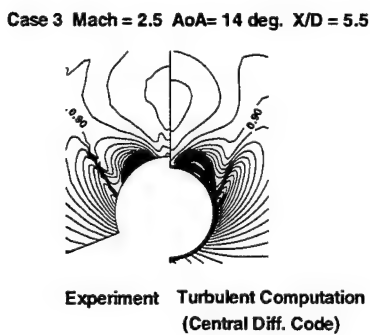


Figure 48: Comparison of Pitot Pressure for Case 3 at $X/D = 5.5$ (Turbulent)

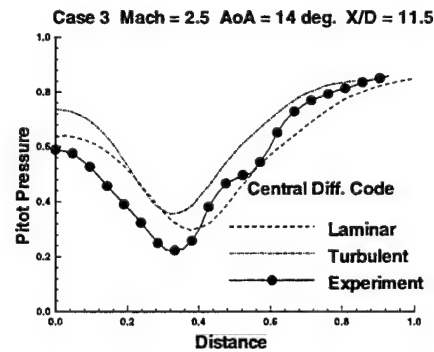


Figure 51: Comparison of Pitot Pressure along Vortex Centerline for Case 3 at $X/D = 11.5$

Case 4 Mach = 3.5 AoA = 8 deg. X/D = 11.5

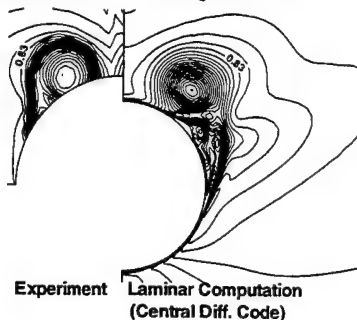


Figure 52: Comparison of Pitot Pressure for Case 4 at X/D = 11.5 (Laminar)

Case 5 Mach = 3.5 AoA = 14 deg. X/D = 5.5

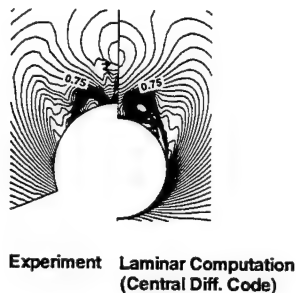


Figure 55: Comparison of Pitot Pressure for Case 5 at X/D = 5.5 (Laminar)

Case 4 Mach = 3.5 AoA = 8 deg. X/D = 11.5

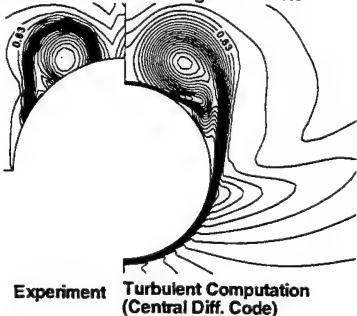


Figure 53: Comparison of Pitot Pressure for Case 4 at X/D = 11.5 (Turbulent)

Case 5 Mach = 3.5 AoA = 14 deg. X/D = 5.5

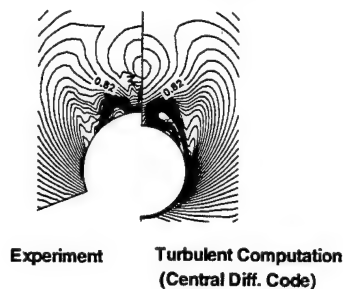


Figure 56: Comparison of Pitot Pressure for Case 5 at X/D = 5.5 (Turbulent)

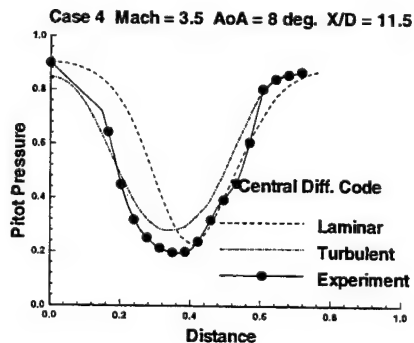


Figure 54: Comparison of Pitot Pressure along Vortex Centerline for Case 4 at X/D = 11.5

Case 5 Mach = 3.5 AoA = 14 deg. X/D = 11.5

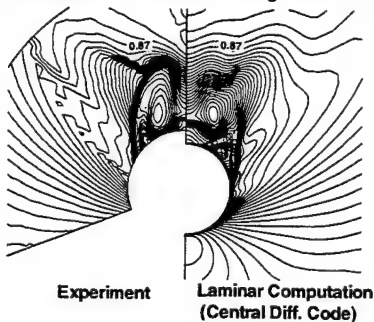


Figure 57: Comparison of Pitot Pressure for Case 5 at X/D = 11.5 (Laminar)

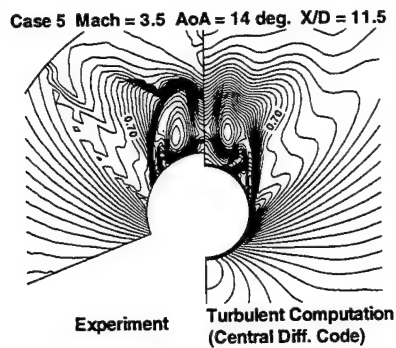


Figure 58: Comparison of Pitot Pressure for Case 5 at $X/D = 11.5$ (Turbulent)

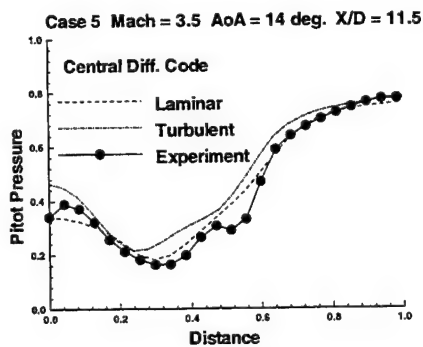


Figure 59: Comparison of Pitot Pressure along Vortex Centerline for Case 5 at $X/D = 11.5$

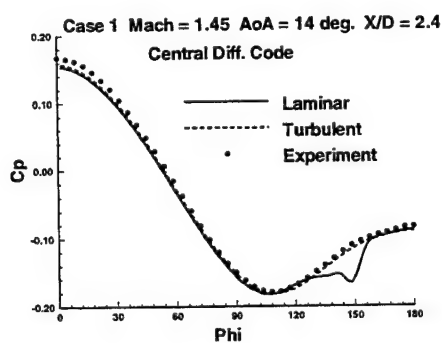


Figure 60: Comparison of Surface Pressure for Case 1 at $X/D = 2.4$

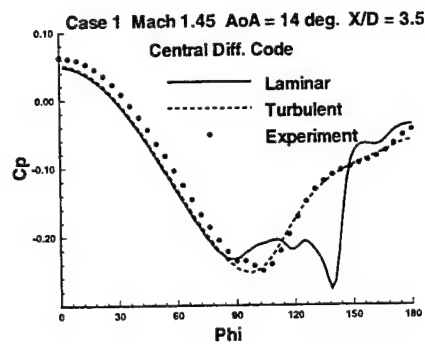


Figure 61: Comparison of Surface Pressure for Case 1 at $X/D = 3.5$

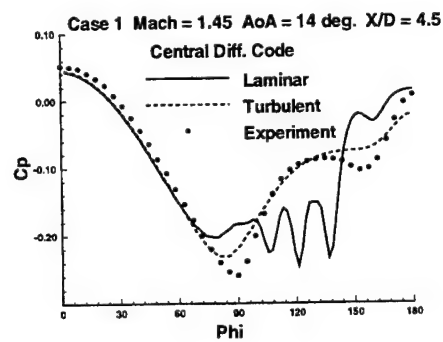


Figure 62: Comparison of Surface Pressure for Case 1 at $X/D = 4.5$

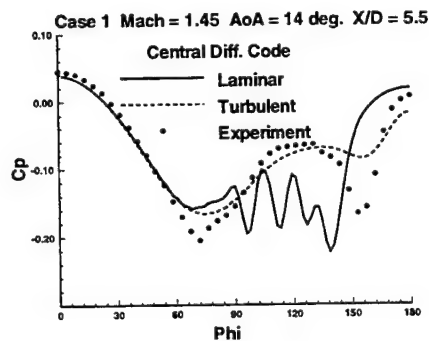


Figure 63: Comparison of Surface Pressure for Case 1 at $X/D = 5.5$

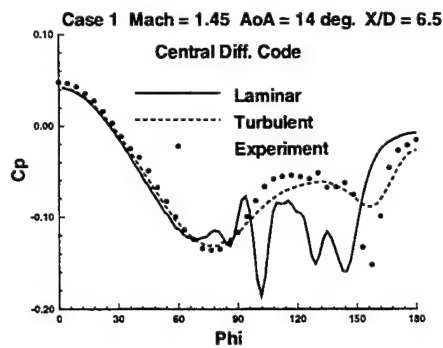


Figure 64: Comparison of Surface Pressure for Case 1 at X/D = 6.5

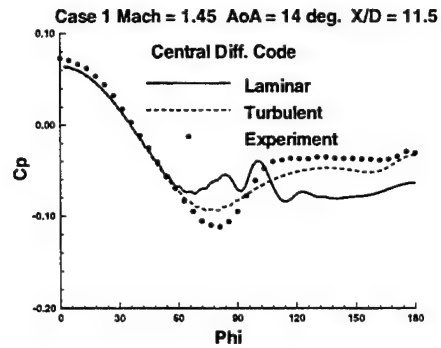


Figure 67: Comparison of Surface Pressure for Case 1 at X/D = 11.5

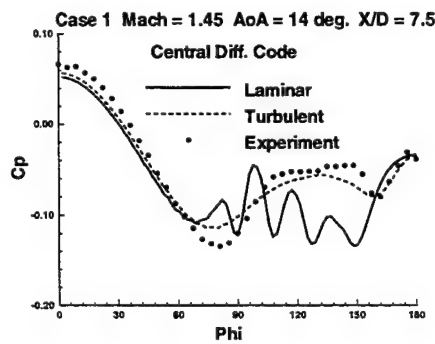


Figure 65: Comparison of Surface Pressure for Case 1 at X/D = 7.5

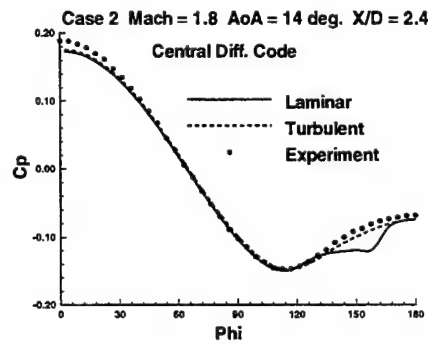


Figure 68: Comparison of Surface Pressure for Case 2 at X/D = 2.4

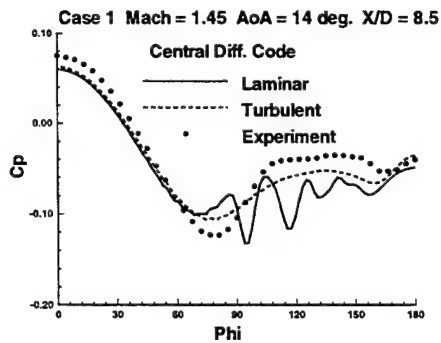


Figure 66: Comparison of Surface Pressure for Case 1 at X/D = 8.5

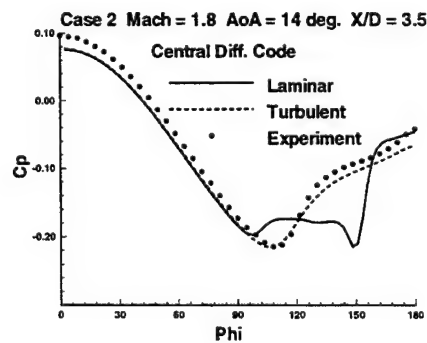


Figure 69: Comparison of Surface Pressure for Case 2 at X/D = 3.5

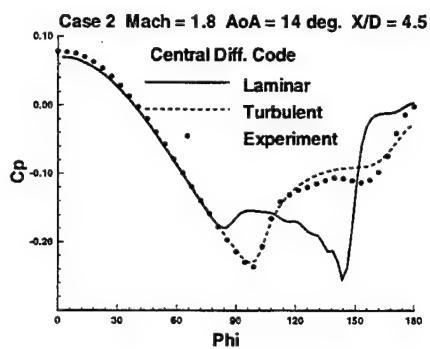


Figure 70: Comparison of Surface Pressure for Case 2 at $X/D = 4.5$

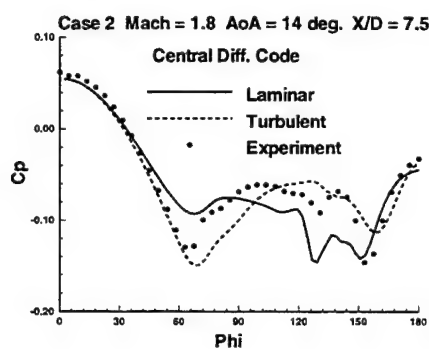


Figure 73: Comparison of Surface Pressure for Case 2 at $X/D = 7.5$

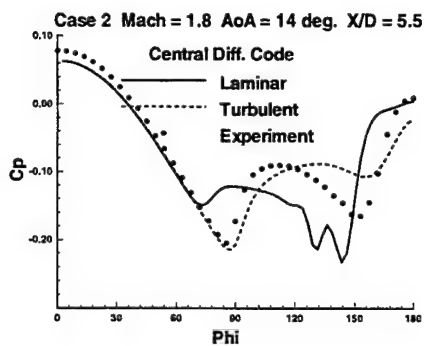


Figure 71: Comparison of Surface Pressure for Case 2 at $X/D = 5.5$

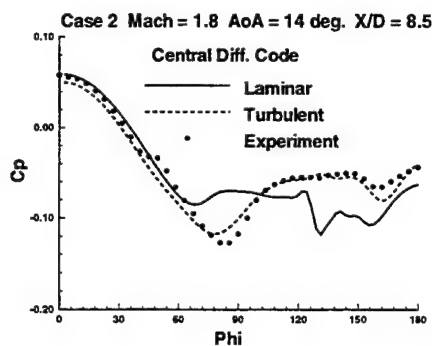


Figure 74: Comparison of Surface Pressure for Case 2 at $X/D = 8.5$

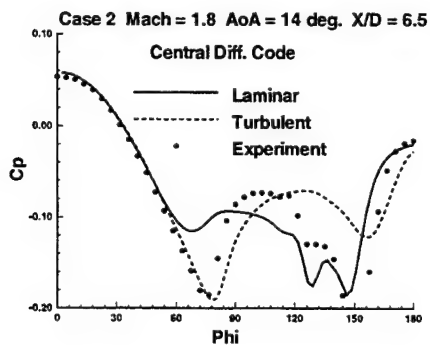


Figure 72: Comparison of Surface Pressure for Case 2 at $X/D = 6.5$

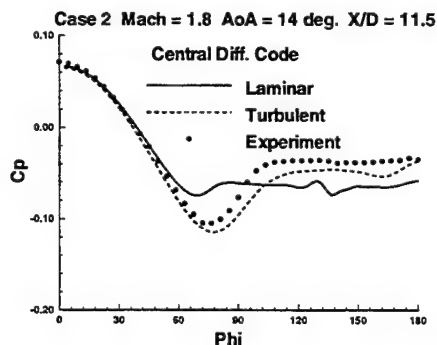


Figure 75: Comparison of Surface Pressure for Case 2 at $X/D = 11.5$

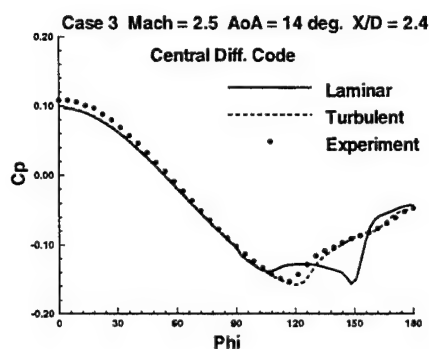


Figure 76: Comparison of Surface Pressure for Case 3 at $X/D = 2.4$

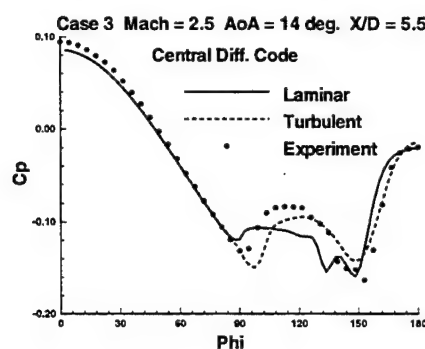


Figure 79: Comparison of Surface Pressure for Case 3 at $X/D = 5.5$

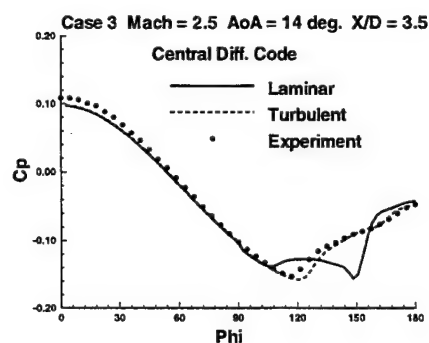


Figure 77: Comparison of Surface Pressure for Case 3 at $X/D = 3.5$

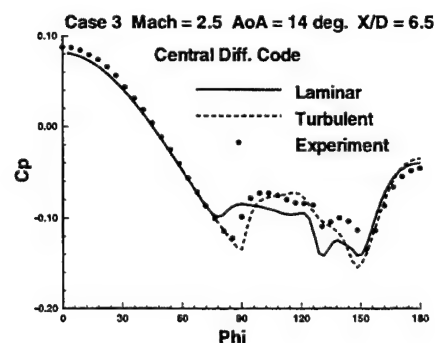


Figure 80: Comparison of Surface Pressure for Case 3 at $X/D = 6.5$

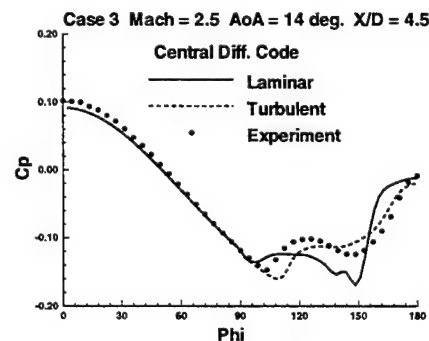


Figure 78: Comparison of Surface Pressure for Case 3 at $X/D = 4.5$

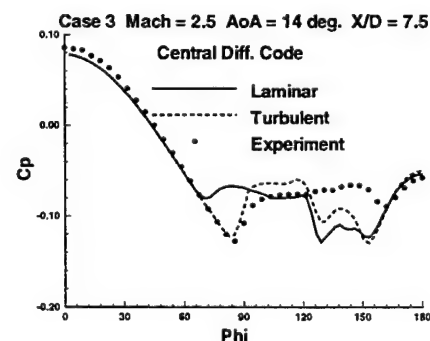


Figure 81: Comparison of Surface Pressure for Case 3 at $X/D = 7.5$

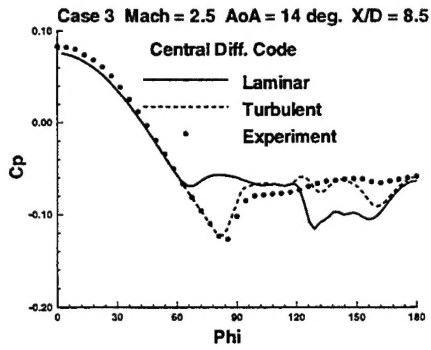


Figure 82: Comparison of Surface Pressure for Case 3 at $X/D = 8.5$

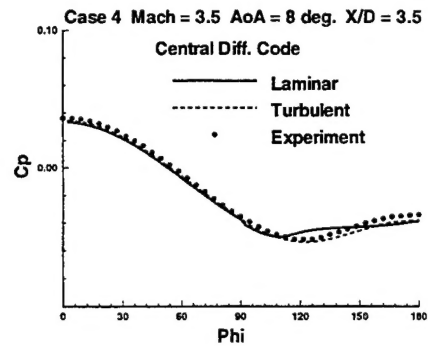


Figure 85: Comparison of Surface Pressure for Case 4 at $X/D = 3.5$

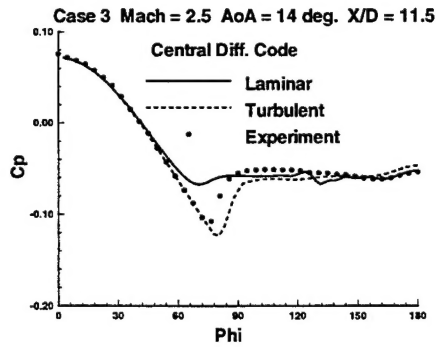


Figure 83: Comparison of Surface Pressure for Case 3 at $X/D = 11.5$

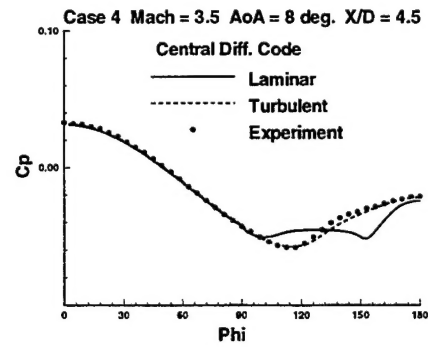


Figure 86: Comparison of Surface Pressure for Case 4 at $X/D = 4.5$

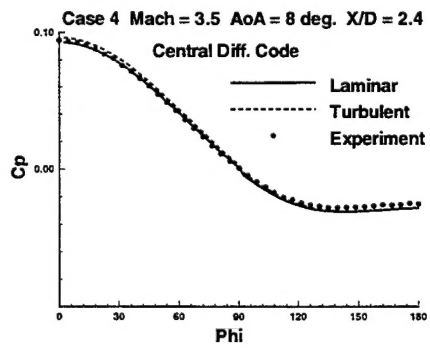


Figure 84: Comparison of Surface Pressure for Case 4 at $X/D = 2.4$

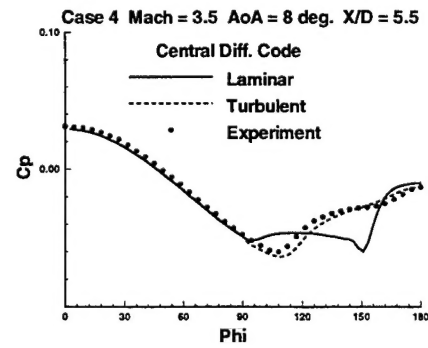


Figure 87: Comparison of Surface Pressure for Case 4 at $X/D = 5.5$

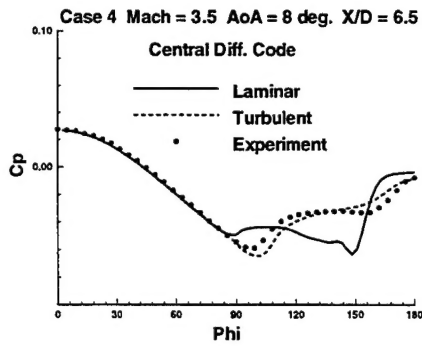


Figure 88: Comparison of Surface Pressure for Case 4 at X/D = 6.5

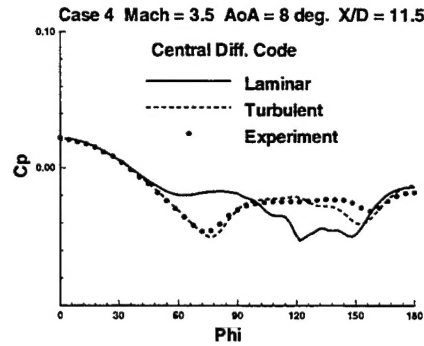


Figure 91: Comparison of Surface Pressure for Case 4 at X/D = 11.5

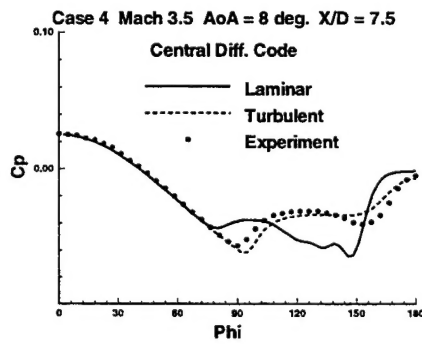


Figure 89: Comparison of Surface Pressure for Case 4 at X/D = 7.5

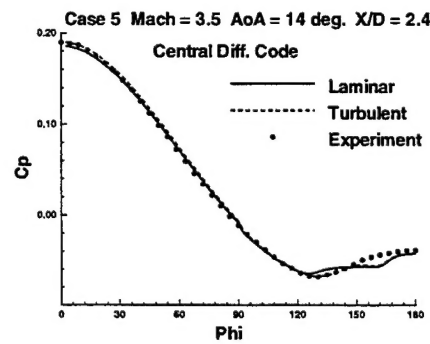


Figure 92: Comparison of Surface Pressure for Case 5 at X/D = 2.4

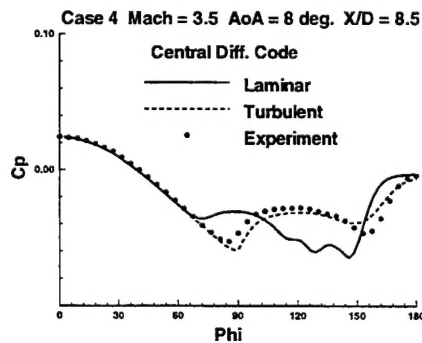


Figure 90: Comparison of Surface Pressure for Case 4 at X/D = 8.5

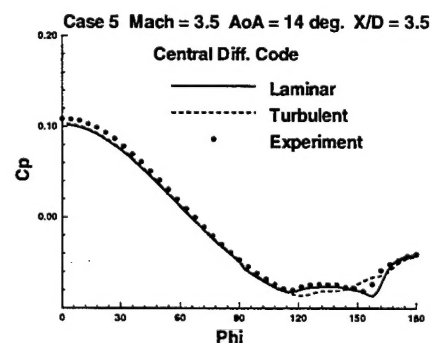


Figure 93: Comparison of Surface Pressure for Case 5 at X/D = 3.5

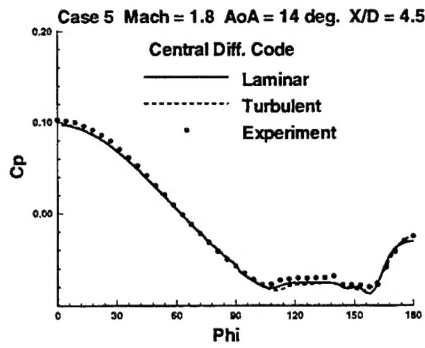


Figure 94: Comparison of Surface Pressure for Case 5 at $X/D = 4.5$

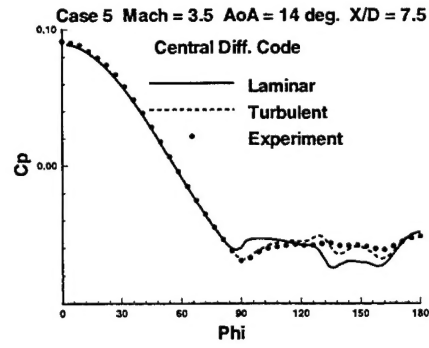


Figure 97: Comparison of Surface Pressure for Case 5 at $X/D = 7.5$

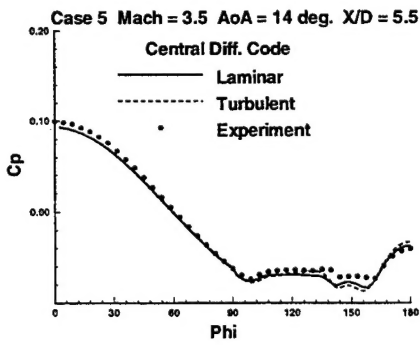


Figure 95: Comparison of Surface Pressure for Case 5 at $X/D = 5.5$

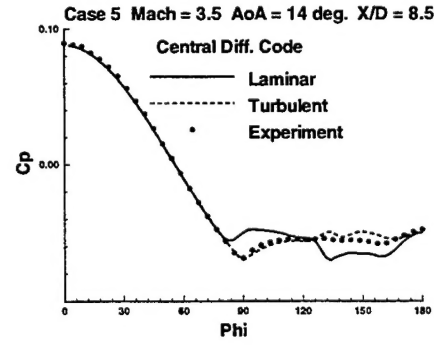


Figure 98: Comparison of Surface Pressure for Case 5 at $X/D = 8.5$

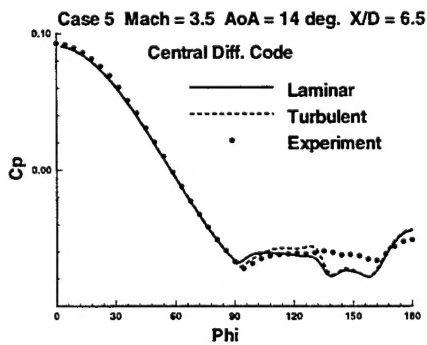


Figure 96: Comparison of Surface Pressure for Case 5 at $X/D = 6.5$

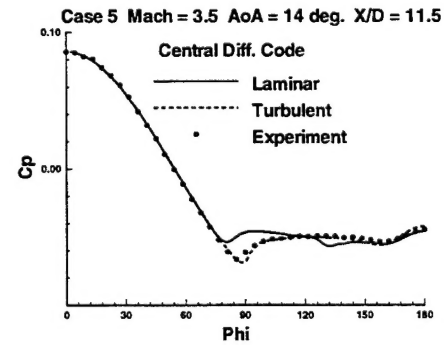


Figure 99: Comparison of Surface Pressure for Case 5 at $X/D = 11.5$

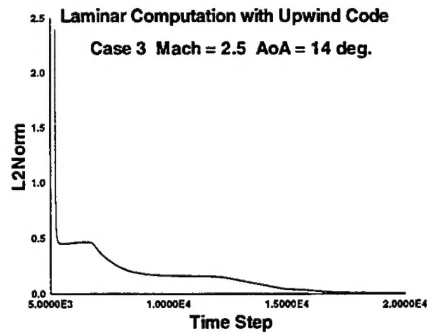


Figure 100: Convergence History for Laminar Computation

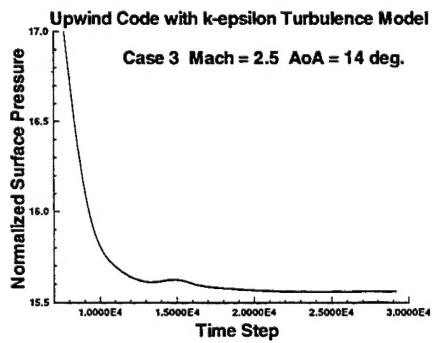


Figure 101: Convergence History for Turbulent Computation